J. Fluid Mech. (2011), *vol.* 687, *pp.* 540–570.
doi:10.1017/jfm.2011.389

A parametric study of breaking bow waves using a 2D + T Technique

Eric Maxeiner†‡, Mostafa Shakeri§ and James H. Duncan

Department of Mechanical Engineering, University of Maryland, College Park, MD 20742, USA

(Received 4 January 2011; revised 10 June 2011; accepted 9 September 2011;
first published online 14 October 2011)

A mechanical two-dimensional wave maker with a flexible surface was used to create waves similar to those formed at the bow of a moving ship. Utilizing the two-dimensional plus time (2D + T) approximation, the wave maker was programmed so that its deformable wave board created a time sequence of shapes that simulated the line of intersection between one side of the hull of a slender ship model moving at constant speed and an imaginary vertical plane oriented normal to the ship model track. However, instead of simulating a particular ship hull, the wave maker was set to produce a parametric set of flat plate motions that represent components of typical bow shapes. The resulting surface waves were measured using a cinematic laser-induced fluorescence technique and the resulting wave profiles were analysed. A large variation of wave crest shapes was observed. An assortment of wave characteristics including the maximum contact point height, maximum wave height and plunging jet geometry were measured and related to the corresponding wave maker motion parameters. Despite the variety of wave maker motions and resulting wave crest shapes, it was observed that the gross parameters describing the wave, such as the maximum wave height, maximum contact point height and wave phase speed, correlate strongly with the wave maker velocity along the water line. Details of the crest shape at the moment of incipient breaking showed a stronger dependence on the initial acceleration of the wave board.

Key words: surface gravity waves, wave breaking, wave–structure interactions

1. Introduction

Waves generated by ships moving through calm water are an important concern for ship designers for several reasons. First, these waves are a major source of ship resistance. Second, when these waves break, usually near the bow and stern, they entrain air bubbles into the water which in turn create white-water wakes. These wakes can contribute to the detectability of the ship via sensors in aircraft and satellites (Peltzer 1984). Finally, the air bubbles entrained by the breakers create significant underwater noise which also contributes to the ship's detectability via underwater acoustic sensors.

† Email address for correspondence: eric.maxeiner.ctr@nrl.navy.mil

‡ Present address: Naval Research Laboratory, Coastal and Ocean Remote Sensing Branch, Washington, DC 20375, USA

§ Present address: Department of Electrical and Computer Engineering, University of Louisville, Louisville, KY 40292, USA

Ship–wave patterns at the model scale are routinely measured during testing of hull designs and these measurements are used to estimate the wave drag on the model. Typical wave pattern measurements consist of wave cuts, i.e. measurements of wave height versus time at fixed locations as the model passes by, and the distribution of the height of the water contact line along the model hull. In addition, qualitative visualization techniques using aluminum powder and tracer particles on the water surface are also employed, and these latter methods can detect wave breaking, see for example Inui (1981), an article summarizing years of research at the Tokyo University Towing Tank. None of these methods, however, can give detailed information about the shape and flow structure of the breakers in the bow region.

Several studies have reported on detailed flow fields in breaking bow waves. Early experimental studies used multi-holed Pitot tubes to measure the mean flow as it passes through spilling breaking bow waves, see for example Miyata (1980), Inui (1981), Aoki *et al.* (1982) and Miyata & Inui (1984). More recently, particle image velocimetry (PIV) measurements in breaking bow waves have been performed by Dong, Katz & Huang (1997) and Roth, Mascenik & Katz (1999). Similar measurements in the bow wave of a surface piercing strut were reported by Pogozelski, Katz & Huang (1997). At the speeds and model scales of all three of these experiments, spilling breakers were formed and the vorticity and energy dissipation in these waves were explored. Also, Olivieri *et al.* (2007) performed PIV measurements in cross-stream planes behind breaking bow waves and explored the relationship between streamwise vortices and deformations of the free surface. Recent numerical computations have addressed breaking bow waves. Dommermuth *et al.* (2006) performed simulations of the flow field around a ship model using an immersed-body and volume-of-fluid method that is able to compute flows with spilling and plunging breakers at the bow. Olivieri *et al.* (2007) found similar results using a Reynolds-averaged Navier–Stokes (RANS) method and give details of the vortical flow created by the breakers.

A simplified bow shape, defined herein as a wedge-shaped bow, can be created from two flat plates that intersect along a straight line at the stem of the ship. The plates may be vertical, creating a wall-sided bow with a vertical stem, or tilted, creating a flared bow with a raked stem. The entrance angle of the hull is taken to be small for ships with fine bows. Because this bow shape is described by only a few geometrical parameters, it is well suited to fundamental studies of the effect of bow shape on the resulting waves. A number of researchers have utilized wedge-shaped bows to perform experiments and devise analytical/numerical solutions of the bow wave problem (see for example Ogilvie 1972; Standing 1974; Aoki *et al.* 1982; Fontaine, Faltinsen & Cointe 2000). Several authors have also considered the waves created by a single surface-piercing vertical plate. Theoretical/numerical studies of this flow include calculations for small yaw angles and approximate the flow using a time-varying potential flow in a cross-stream plane with a wall of infinite or finite draft starting from rest and then moving at constant speed, see for example Chapman (1976), Roberts (1987) and Calisal & Chan (1989). An experimental investigation of the flow created by a yawed flat plate was reported by Waniewski, Brennan & Raichlen (2001, 2002). The experiments were performed in a supercritical free-surface flow in a shallow-water flume using a vertical plate whose leading edge was in contact with the sidewall of the flume. Surface profiles of the resulting waves were measured and used to investigate scaling and dependence on geometric parameters. In general, the various profiles, regardless of model scale, were similar near the leading edge of the plate but deviate significantly thereafter.

A series of papers by Noblesse *et al.* (2006, 2008*a*,*b*, 2009, 2011) and Delhommeau *et al.* (2009) used simple analytical expressions combined with experimental data and thin-ship theory to predict bow wave characteristics. A number of relations were developed to predict the height, location and steepness of bow waves as a function of the forward speed, entrance angle, rake and flare of the bow.

Several researchers have employed the 2D + T (two dimensions plus time) approximation for theorectical/numerical studies of ship bow waves, see for example Tulin & Wu (1996), Colagrossi, Landrini & Tulin (2001) and Landrini, Colagrossi & Tulin (2001). In this method, the three-dimensional bow flow is approximated by a two-dimensional, time-evolving flow in which the hull is replaced by a deforming wall which at any time t ($t = 0$ is the moment of passage of the bow stem along the mean water level) takes on the shape of the cross-section of one side of the hull at the streamwise (x) location corresponding to $x = Ut$, where U is the equivalent speed of the three-dimensional ship model (see § 2.1, figure 1). Similar methods were used in the examination of wave generation by yawed flat plates (see Chapman 1976, Roberts 1987 and Calisal & Chan 1989, as discussed above), in high-speed planing flows (Tulin 1957), in high-speed slender displacement hull flows (Tulin & Hsu 1986) and deck wetness flows (Song & Maruo 1993). The 2D + T method is applicable only to ships with fine bows moving at relatively high constant forward speed and only divergent wave components are produced. In these 2D + T simulations there is no predetermined forward speed and therefore several flow phenomena are not accounted for, including the ship boundary layer, vortical flows created by the mean flow over various features of the hull, longitudinal waves and the stagnation point at the bow. The impact of these processes on the bow wave system of fine bowed ships is thought to be relatively weak. Numerical studies using the 2D + T method to simulate bow wave generation by specific hull shapes include Tulin & Wu (1996) and Tulin & Landrini (2000) and similarly directed experimental studies include Shakeri, Tavakolinejad & Duncan (2009*a*) and Shakeri *et al.* (2009*b*). As shown quantitatively in Shakeri *et al.* (2009*a*,*b*), the wave measurements from the 2D + T experiments compare well with the wave measurements in experiments with fine-bowed three-dimensional models at high-Froude-number conditions.

In the present study, the 2D + T wave maker used in Shakeri *et al.* (2009*a*,*b*) is employed to explore the relationship between bow shape (wave maker motion) and breaking bow waves. To this end, the 2D + T wave maker is set to produce motions consisting of various combinations of the translation and rotation of a flat plate. Using the 2D + T transformation, these wave maker motions approximate both families and components of wedge-shaped bows. The waves are examined with a cinematic laser-induced fluorescence (LIF) method that allows for measurements of traditional quantities such as the wave height and the contact point height along the 'hull', but also allows for detailed measurements of the crest shape during breaking which are difficult to obtain with traditional towing-tank tests using three-dimensional models. The results of this study may also be considered in terms of two-dimensional breaking waves produced by the single stroke of a deformable piston-like wave maker. Unlike typically studied two-dimensional deep water breakers as reviewed in Banner & Peregrine (1993), Melville (1996) and Duncan (2001), the waves in the present study are highly forced with some of them breaking as they are being formed adjacent to the flexible surface of the wave maker.

The remainder of this paper is divided into three sections. The details of the experimental setup and measurement techniques are given in the following § 2. This is

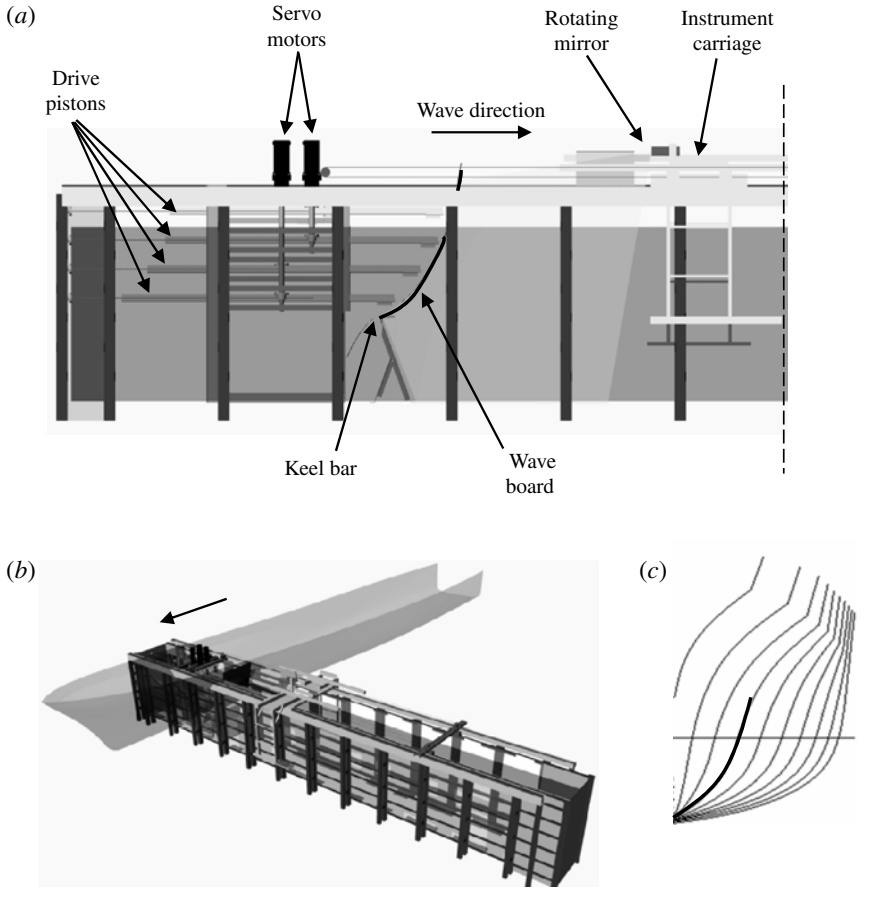

FIGURE 1. Overview of experimental setup and 2D + T technique. (*a*) Side view of the wave tank, 2D + T wave maker and instrument carriage. (*b*) Perspective view of the wave tank with imaginary ship hull moving in the direction perpendicular to the long axis of the tank. (*c*) Set of profiles of the port side of a typical ship hull at various streamwise sections from stem to midships. During a typical run, the wave board undergoes a sequence of shapes matching the set of profiles shown in (*c*). These profiles are equivalent to the lines of intersection of the port side of the imaginary ship hull and the sidewall of the tank as the hull moves through the tank at constant speed.

followed by a description and discussion of the results in § 3. Finally, the conclusions are given in § 4.

2. Experimental details

2.1. *Experimental facilities*

A detailed description of the experimental facilities used in this study can be found in Shakeri *et al.* (2009*a*). A brief overview of these facilities is given below for the sake of completeness. A schematic drawing of the wave tank and the 2D + T wave maker is shown in figure 1. The tank is 14.80 m long, 1.15 m wide and 2.20 m deep. The wave maker, which occupies about 2.8 m of the tank length at one end, is powered by four servomotors. These servomotors drive four vertically oriented shafts that, in turn, drive four horizontal pistons through separate rack-and-pinion assemblies. The

main component of the 2D + T wave maker is a set of interleaved flexible stainless steel plates, hereby referred to as the wave board. The wave board is driven by four drive plates which are individually bolted to the four drive pistons. Each drive plate is attached to a separate layer of the wave board via hinges. Manipulating the sequences of positions and velocities of each drive piston forces the wave board to bend and translate to create a desired sequence of shapes. As the pistons move out at different speeds, the changing distance between the hinge points is accommodated by the stainless steel plates sliding relative to each other. Four position sensors, one for each drive piston, provide data for a computer-controlled feedback system. The feedback system adjusts the velocity of each drive piston in real time to achieve the desired wave board motion. An instrument carriage is mounted on top of the tank. The carriage is driven by towing cables which, in turn, are powered by a servomotor. The wave board and the carriage motions are synchronized via a central computer.

The keel depth of the 2D + T wave maker is established by bending the wave board over a fixed horizontal surface, called the keel bar, that spans the width of the tank at a height 0.81 m above the tank floor. The keel depth serves as the effective draft, d, for the model. For all tests in this study, the mean water depth was fixed at 0.892 m above the top surface of the keel bar for a total water depth of 1.70 m.

As shown in figure 1, the wave board is extended and bent at each time, t, so that its shape matches the corresponding half-hull shape at a given longitudinal location (x), given by $x = Ut$, where U is the forward speed of the corresponding three-dimensional ship model and $t = 0$ corresponds to the time of passage of the ship stem. Typically, an experimental run simulates the passage of the model hull from stem to midships. The portion of the hull aft of midships is assumed to be effectively parallel. Even if this aft portion of the hull is not parallel on the three-dimensional ship model, its shape will have negligible influence on the bow waves and can be safely ignored.

As the length of any gravity wave decreases, the kinetic energy of the flow decreases and the effect of surface tension becomes more important. The relative importance of surface tension can affect the shape of the wave crest and plunging jet as well as the turbulent flow and free surface motions in the splash zone, see for example Brocchini & Peregrine (2001). One advantage of the present 2D + T experimental setup is the relatively large model scale and corresponding long wavelength of the simulated bow waves. For example, Shakeri *et al.* (2009*b*) were able to test at a scale ratio of 1/2.4 whereas the equivalent three-dimensional model tests discussed in that paper were performed at a scale ratio of 1/8.25. As a result, the waves produced using the 2D + T setup were over three times larger than those produced in the three-dimensional model tests.

2.2. *Wave maker motion categories*

The goal of this study is to determine the relationship between generic, quantifiable wave maker motions that simulate fundamental components of ship bows and the resulting breaking waves. In all of the wave board motions used in this study, the wave board, with the exception of the region close to the keel bar, maintained the shape of a flat plate. Five categories of wave board motions were used (see figure 2). The first is rotation about the keel bar (hereafter called 'Slap'). The second category (called 'Fixed') is horizontal translation of the wave board while it is maintained at a fixed angle, θ, which is measured from vertical. The remaining three categories, 'Mix 0.2', 'Mix 0.4' and 'Full', employ simultaneous rotation and translation. In these cases, rather than a stationary centre of rotation at the keel bar as in the Slap motion, the centre of rotation translates horizontally and is located at the point where the

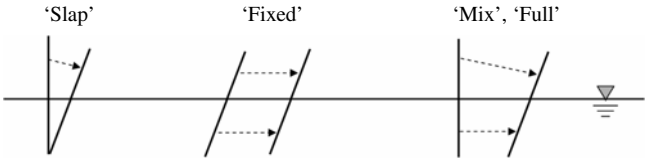

FIGURE 2. Graphical representations of the wave maker motion categories used in this study.

imaginary extension of the flat part of the wave board crosses the keel bar depth. The term 'Full' is used because this wave board motion incorporated the largest translation the wave maker would allow (1.152 m at the waterline). The 'Mix' categories have shorter translations than the Full category, effectively making them intermediaries between the Slap and the Full categories (i.e. a *mix* between the Slap and the Full). Bottom translation is denoted by B_k, which relates to the hull beam at the keel depth. In the 2D + T wave maker, bottom translation results in tight curvature of the wave board near this depth due to the presence of the keel bar. While this curvature is a slight deviation from a flat-plate motion, its takes place well below the mean water surface (about 0.6 m below) and likely has negligible effects on the waves generated. The Slap cases have no bottom translation and thus the wave board is completely flat throughout the motion. The Mix 0.2 and Mix 0.4 categories have B_k values of approximately 0.2 m and 0.4 m, respectively. The Slap, Mix and Full categories can all be thought of as being part of the same family of motions (rotating) and the Fixed category constitutes a second family (translation only). As we show throughout this paper, many of the wave characteristics seem to behave according to these two families of motions, i.e. the Fixed cases often behave slightly differently than the rest of the cases.

The rotation and translation motions of the wave board simulate fundamental components of ship bow shapes. The equivalent hull shapes that would be represented by the Slap, Full and Fixed categories are shown in figure 3 along with a typical naval surface combatant hull. As can be seen in the figure, even though the wave maker motions are simple, quantifiable combinations of translation, rotation and board angle, they do approximate ship-like shapes. The Full motion appears to most closely resemble a typical hull. The Fixed motion is anomalous in the sense that the equivalent hull lacks any sort of stem, i.e. the wave maker starts at a position that is already translated along the waterline. While this is obviously not a feasible hull shape, it allows for translation and board angle to be analysed independently of rotation.

Owing to the generic nature of the wave maker motions, there is no particular equivalent full-scale ship length and thus no model size or scaling factor. The draft/beam ratio is fixed for a given wave maker motion category but the corresponding slenderness (length/beam or length/draft ratio) may be selected arbitrarily. Thus, the corresponding forward velocity of the hull is also arbitrary in the sense that it is directly related to the chosen slenderness.

As discussed above, the wave maker motion categories simulate a variety of approximate bow shapes and are not restricted to a particular slenderness ratio or even a particular forward speed. Thus, in contrast to studies evaluating the waves generated by a single hull design, the results of this study highlight the relationship between some fundamental components of bow shape and the waves produced.

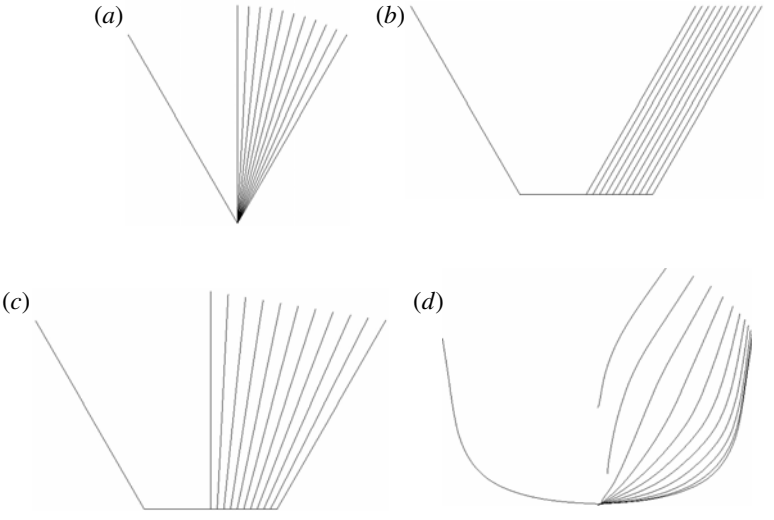

FIGURE 3. Illustration of wave maker motion categories as three-dimensional hull forms. Equivalent idealized hull section lines are shown for (*a*) Slap, (*b*) Fixed ($\theta = 30°$), (*c*) Full and (*d*) a typical naval combatant hull. Each line represents a cross-section shape spaced at $L/20$ offsets, where L is notional ship length. Each hull form is assumed to be parallel after the midship.

2.3. *Wave-maker drive-piston motion profiles*

The various motions of the wave board are created by the motions of the four drive pistons. The idealized motion of each piston is a region of constant velocity connecting the stationary start and end positions. However, because the wave maker is a mechanical device, discontinuous velocities, i.e. infinite accelerations, are not possible and overly high accelerations may cause errors or damage to the system. For this reason, the corners at the two ends of the constant velocity zone of the drive-piston position-versus-time profiles must be smoothed. Thus, in the motion profiles used herein (see figure 4), the acceleration (deceleration) at the beginning (end) of the motions profile increases (decreases) linearly from zero to a maximum (minimum) value and then back to zero again, as shown in figure 4(*a*). In the idealized, i.e. discontinuous-velocity, motion profiles, the run begins at $t = 0$ and ends at $t = t_{wm}$, where t_{wm} is the wave maker run time. In the motion profiles used herein, as shown in figure 4(*b*), $t = 0$ and $t = t_{wm}$ are taken as the times of maximum acceleration and deceleration, respectively, with the acceleration occurring between $t = -0.5T_R t_{wm}$ and $t = 0.5T_R t_{wm}$ and the deceleration occurring between $t = (1 - 0.5T_R)t_{wm}$ and $t = (1 + 0.5T_R)t_{wm}$, where T_R is a non-dimensional input parameter called the rounding period. For a set of runs with the same run time (t_{wm}) and maximum wave board speed (V_b), the maximum and average acceleration increase as T_R is decreased. Unless specified otherwise, $T_R = 0.5$ throughout this study, including in figure 4. The effects of T_R on the wave profiles will be examined further in § 3.4. A set of profiles of position versus time for the four wave maker drive channels for a typical wave maker motions used in this study is given in figure 5. Both the idealized (dashed lines) and smoothed (solid lines) profiles are shown. As can be seen in figure 5, the differences between the idealized and smoothed position-versus-time profiles are relatively small.

Given the common set of motion profiles of the drive pistons as described above, the motions of the wave board can be described by a limited set of parameters. For

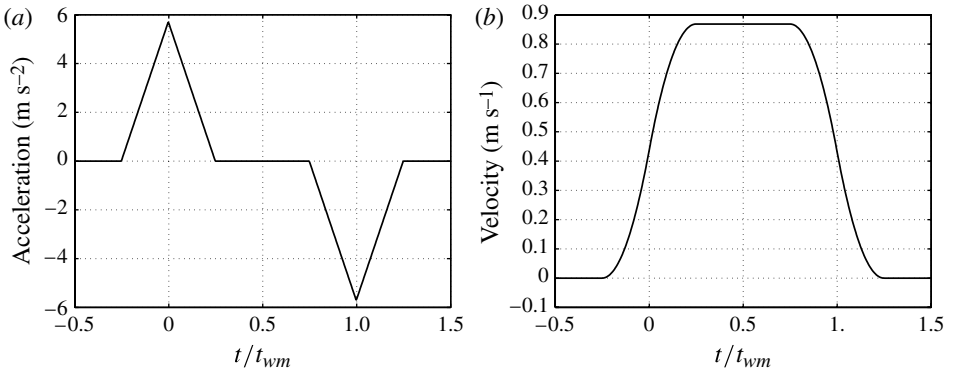

FIGURE 4. Typical profiles of acceleration (*a*) and velocity (*b*) for a single wave maker drive piston for a typical wave maker motion, with time normalized by t_{wm}.

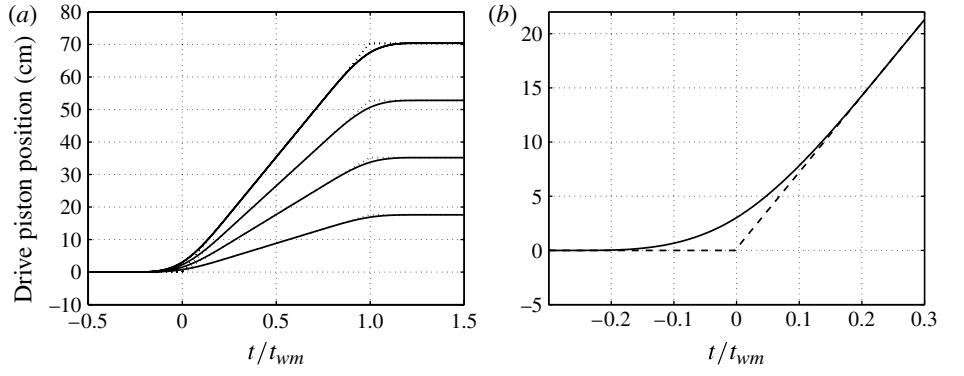

FIGURE 5. (*a*) Position histories for all four wave maker channels for a typical wave maker motion profile. The drive piston positions are the horizontal distance from the starting position of each piston. The solid lines indicate the actual profiles and the dashed lines indicate the idealized (infinite acceleration) profiles. (*b*) Close-up view of a typical initial acceleration for one of the channels.

the Slap, Mix and Full categories, all of which include a rotation of the wave board, these parameters are the draft, d, the wave board horizontal displacement at the keel depth, B_k, the run time, t_{wm}, the angular displacement of the wave board, $\Delta\theta$, and the above-described rounding time ratio, T_R. For the motions in the Fixed category, the list is as above, but with $\Delta\theta$ replaced by θ, the fixed wave board angle. In this set of motion parameters, we can also replace B_k with B_w (the wave board displacement at the mean water level) since in all cases $B_w = B_k + d\tan\Delta\theta$ (with $\Delta\theta = 0$ in the Fixed cases).

The above list can be further modified by using the wave board speed (V_b) and acceleration (a_b). The wave board speed is defined as the maximum wave board horizontal speed at the height of the undisturbed waterline during an experimental run. For the Fixed cases, every point on the wave board moves at the same velocity whereas the rotational motion component in the Slap, Mix and Full cases results in greater velocities at higher elevations, i.e. farther above the keel bar. Given the

above-described motion profiles, it can be shown that

$$V_b = \frac{B_w}{t_{wm}} \tag{2.1}$$

in all cases. The wave board acceleration, a_b, is defined as the average horizontal component of the acceleration at the height of the undisturbed waterline during the initial acceleration period. For the motions in this study, the acceleration profile is triangular (see figure 4*a*), thus, the average acceleration is simply half of the maximum acceleration. From the above-described motion profiles it can be shown that

$$a_b = \frac{B_w}{T_R t_{wm}^2} = \frac{V_b}{T_R t_{wm}}. \tag{2.2}$$

Using the above definitions, we can create a final list of independent variables:

$$(d, V_b, a_b, (\theta \text{ or } \Delta\theta), T_R) \tag{2.3}$$

where we have replaced B_k and t_{wm} with V_b and a_b. Finally, V_b is usually given in dimensionless form as the wave board Froude number,

$$F_b = \frac{V_b}{\sqrt{gd}}. \tag{2.4}$$

Because the draft is held constant ($d = 0.892$ m) for all cases, $F_b = 0.338V_b$ when V_b is expressed in metres per second.

Most of the wave board parameters are readily comparable to ship parameters. For example, the wave board speed V_b, can be calculated using the ship speed, U and the entrance angle, $2\alpha_E$, from the relationship $V_b = U \tan \alpha_E$. Thus, wave characteristics that show a strong dependence on V_b would show a strong dependence on U for a given bow shape. The wave board angle, θ, is directly related to the bow flare angle, thus, for instance, the results from the runs in the Fixed motion category examine the effect of fixed flare angle. Also, the 2D + T wave maker draft is directly comparable to the draft of the ship. One difference between the 2D + T equivalent bow shape and the shape of a ship bow concerns the finite initial acceleration of the wave board, characterized by a_b. As pointed out in Shakeri *et al.* (2009*a*), the finite initial acceleration creates a sharply pointed stem on the equivalent three-dimensional model, while the stem on a ship is a rounded for structural reasons. Although the equivalent stem shape and the ship stem shape have this difference, it is hypothesized that the acceleration parameter may mimic the cross-stream acceleration seen by fluid particles as they approach and pass around the stem in the real three-dimensional flow which is related in some complex way to the bow shape and forward speed of the ship.

2.4. *Wave measurements*

A cinematic LIF system, identical to that described in detail by Shakeri *et al.* (2009*a*), was used to measure the temporal history of the profiles of the waves generated by the 2D + T wave maker. A simplified description of this system is given below for completeness; the interested reader is referred to the original reference for details.

In the LIF system, a light sheet from a 6 W argon-ion laser is directed downwards along the centre plane of the tank from above the water surface, see figure 6. The water in the tank is mixed with fluorescein dye at a concentration of about 5 ppm. The glowing dye at the intersection of the light sheet and the water surface is photographed using a digital high-speed movie camera (Phantom 9.0, Vision Research, Inc.) which

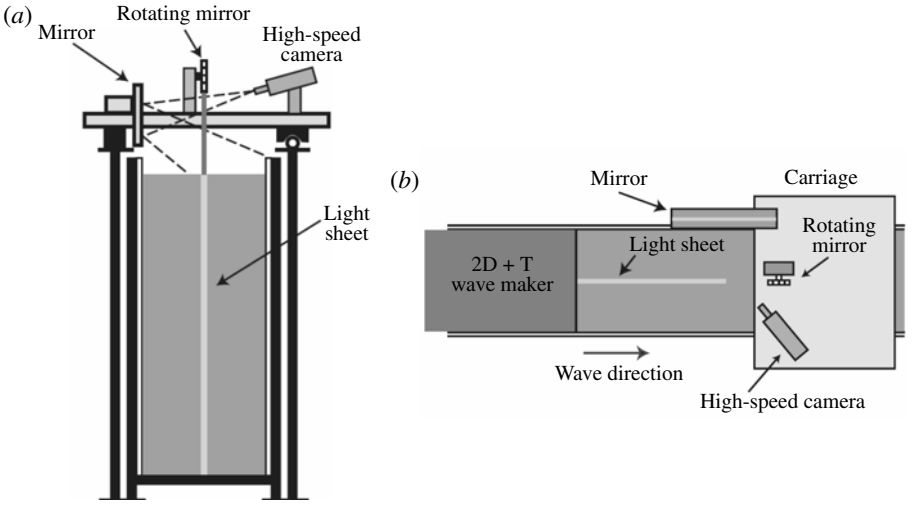

FIGURE 6. Details of the optical setup. A longitudinal view (looking away from the wave maker) is shown in (*a*) and an overhead view is shown in (*b*).

is set to take 256 images per second and is mounted on the instrument carriage along with the rotating mirror used to create the laser light sheet. The carriage is set to move with the same motion as the top drive piston of the wave maker and the camera is synchronized with the wave maker and carriage motions. The glowing dye at the intersection of the water surface and the laser light sheet creates a sharp, clearly visible black-to-white edge in the images. A gradient-based algorithm is used to trace this edge in each wave image. The resulting water surface profile is in the image coordinate system with units of pixels. In order to transform the surface profile into physical space, an inverse mapping procedure is employed. Before and after every set of tests, images of a large black-and-white checkerboard, which is placed in the plane of the laser light sheet in the tank (see figure 7), are recorded with the camera in the same position and orientation as when surface profile measurements are taken. The checkerboard images are used to map image coordinates into physical coordinates. The origin of the physical coordinates, hereby referred to as the test origin, is taken as the intersection of the undisturbed water surface and the wave board when the wave maker is in its initial position. When considering errors in image calibration, edge detection in the images and determining the carriage position when the image is taken, measurement of the water surface is estimated to have an accuracy of ± 1.3 mm in the physical plane (Shakeri *et al.* 2009*a*).

Figure 8 shows a typical wave image with several of the important features pointed out. Locations of the contact point, crest and jet tip are tracked over time and space. The contact point and jet tip are identified visually from the images whereas the crest location is determined by calculating the point of local maximum height in an individual surface profile.

2.5. *Repeatability*

In general, both the wave maker and the measurement techniques produced very repeatable results. A plot of surface profiles taken at the same times (at 1/16-second intervals) relative to the wave maker motion for three successive runs of the same case (Slap, $V_b = 0.85$ m s^{-1}) is shown in figure 9. The profiles are within 1 mm of

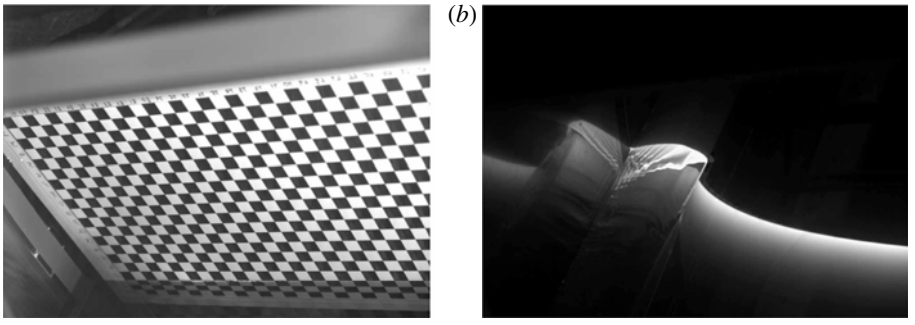

FIGURE 7. Images of (*a*) the calibration board and (*b*) a typical wave. Both images were taken with the same camera position and orientation with respect to the tank. In (*a*), the surface of the calibration board was placed in the same plane as that of the laser light sheet. The checkerboard consists of an array of 2.54 cm squares. The various features of the wave image are pointed out in figure 8.

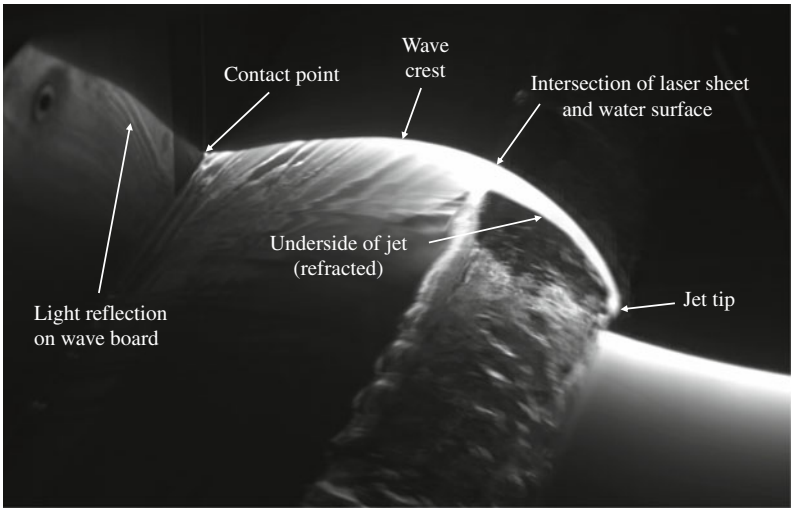

FIGURE 8. Various features of a typical wave image (Slap, $V_b = 0.95$ m s^{-1}).

one another except for the regions around the jet tip and the splash zone where there are only slight deviations due to random fluctuations which appear to be caused by turbulence-induced surface motions. At subsequent times, a large turbulent splash zone appears with large variations in surface profiles from run to run. This splash zone in 2D + T experiments is discussed in Shakeri *et al.* (2009*a*).

2.6. *Test conditions*

Table 1 lists the five wave maker motion categories and the ranges of the key wave maker parameters within each category. The run times, and subsequently the wave maker velocities, were chosen to span the range from breaking inception up to the fastest speeds the wave maker could reproduce without significant position errors or excessive stress to the system. This upper speed limit was not a significant restriction as strong plungers could be produced easily for all motion categories. In all rotating cases (Slap, Mix and Full) the total rotation was 30°. The board angle, θ, for the Fixed

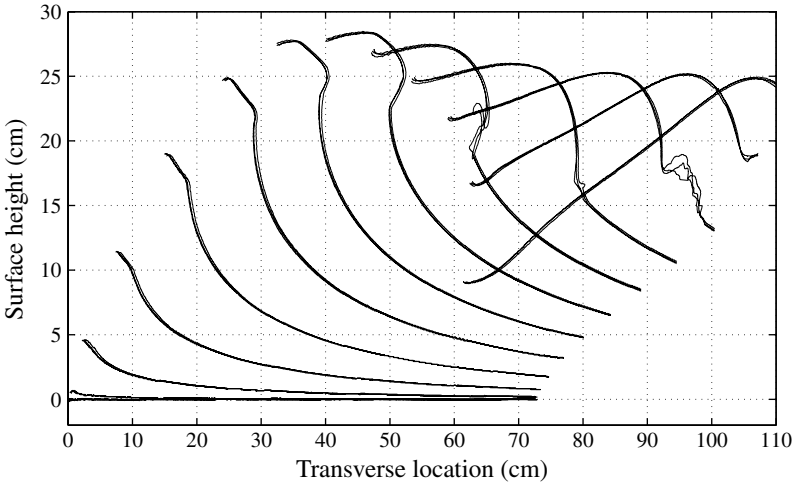

FIGURE 9. Water surface profiles taken at the same times in 1/16 s intervals from three separate of runs of the same wave maker motion (Slap, $V_b = 0.85$ m s^{-1}).

Category	θ_0 (°)	θ_{end} (°)	B_k (m)	B_w (m)	t_{wm} (s)	V_b (m s^{-1})
Slap	0	30	0	0.515	0.54−0.96	0.53−0.95
Mix 0.2	0	30	0.212	0.727	0.75−1.10	0.66−0.97
Mix 0.4	0	30	0.425	0.940	0.98−1.25	0.76−0.96
Full	0	30	0.637	1.152	1.11−1.35	0.85−1.04
Fixed	15, 20, 25, 30	same as θ_0	0.610	0.610	0.65−1.17	0.52−0.94

TABLE 1. Table of wave maker motion parameters for the five categories of wave maker motions, including the range of run times (t_{wm}) and wave board speeds (V_b). The angles θ_0 and θ_{end} are the initial and final angles, respectively, of the wave board relative to vertical. Here B_k and B_w refer to bottom (keel elevation) translation and undisturbed waterline translation of the wave board, respectively.

cases ranged from 15° to 30°. Mechanical limitations did not allow for a zero board angle (i.e. a vertical plate) Fixed case. The maximum board angle of 30° likely limits the applicability to pure-displacement hulls only (i.e. no planing).

3. Results and discussion

3.1. *General observations*

Wave profiles were measured for a total of 46 different wave maker motions, all within the parameters of table 1. Several images from a high-speed LIF movie and the corresponding surface profiles in physical coordinates for a representative Slap wave maker motion with $V_b = 0.78$ m s^{-1} ($t_{wm} = 0.66$ s) are shown in figure 10. Prior to any motion (a and b, $t = -0.17$ s), the water surface is flat and normalized to zero elevation. As the wave board begins to move forward (c and d $t = 0.15$ s), the surface deflects upward in the area near the wave board and a jet is formed moving upward along its surface. As the wave board continues to move, the surface deflection continues to move upward (e and f $t = 0.33$ s) and begins to form a bulge near the

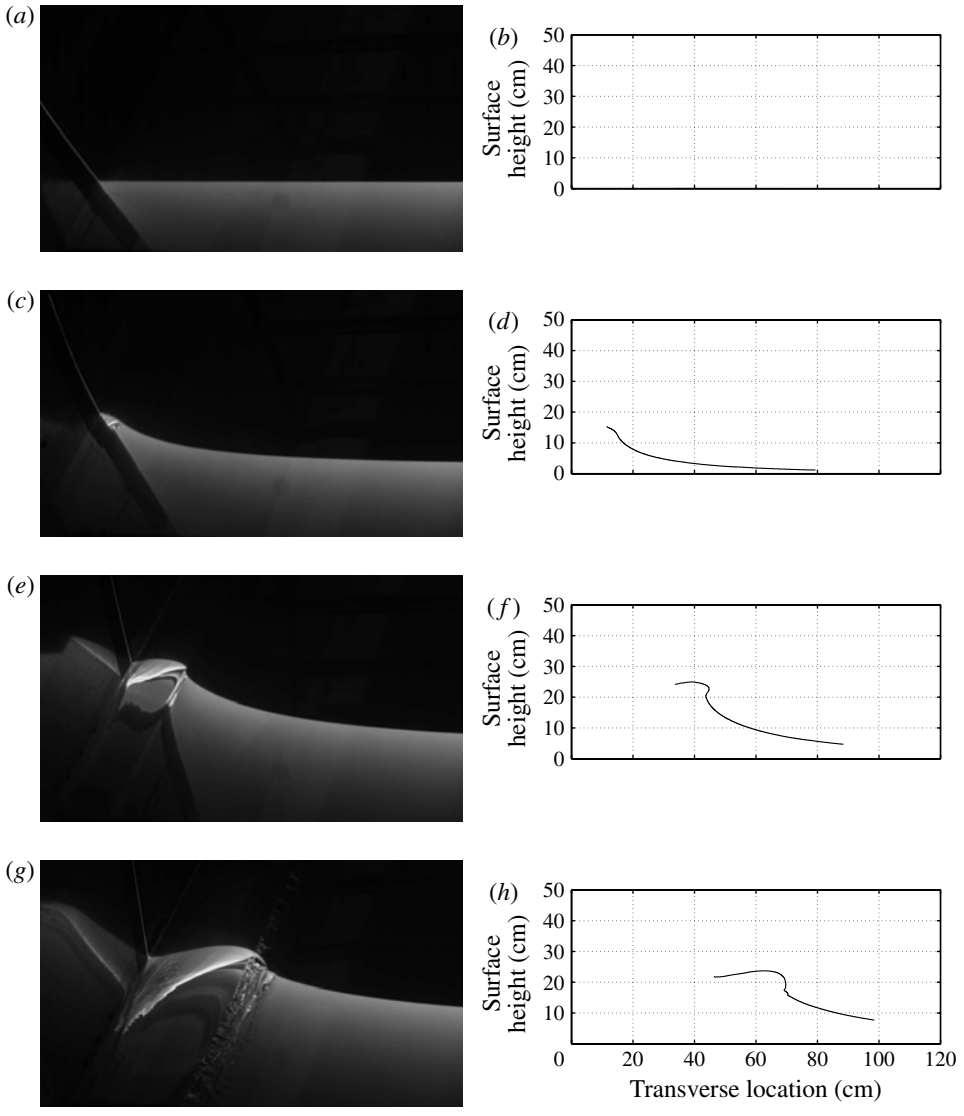

FIGURE 10. Time series of a typical wave profile (Slap, $V_b = 0.78$ m s^{-1}, $t_{wm} = 0.66$ s). The figures in the left-hand column are unprocessed images from the high-speed movies and the figures on the right are the corresponding surface profiles in physical coordinates. The times of the four figure–image pairs are $t = -0.17$, 0.15, 0.33 and 0.46 s, respectively.

location of the maximum water height. After a short time, a wave begins to move away from the wave board and breaks (g and h, $t = 0.46$ s), in this case forming a weak plunger. Comparing the corresponding images and surface profiles shows clearly the optical skewness of the images.

The various wave maker motions produced very different wave shapes. Images taken at the moment of plunging jet impact for six different cases covering all wave maker motion categories are given in figure 11. All cases were run within a relatively narrow range of wave board speeds (between 0.94 and 0.97 m s^{-1}) and all developed clearly defined plunging jets. Note the variation of plunging jet shape, length, thickness and

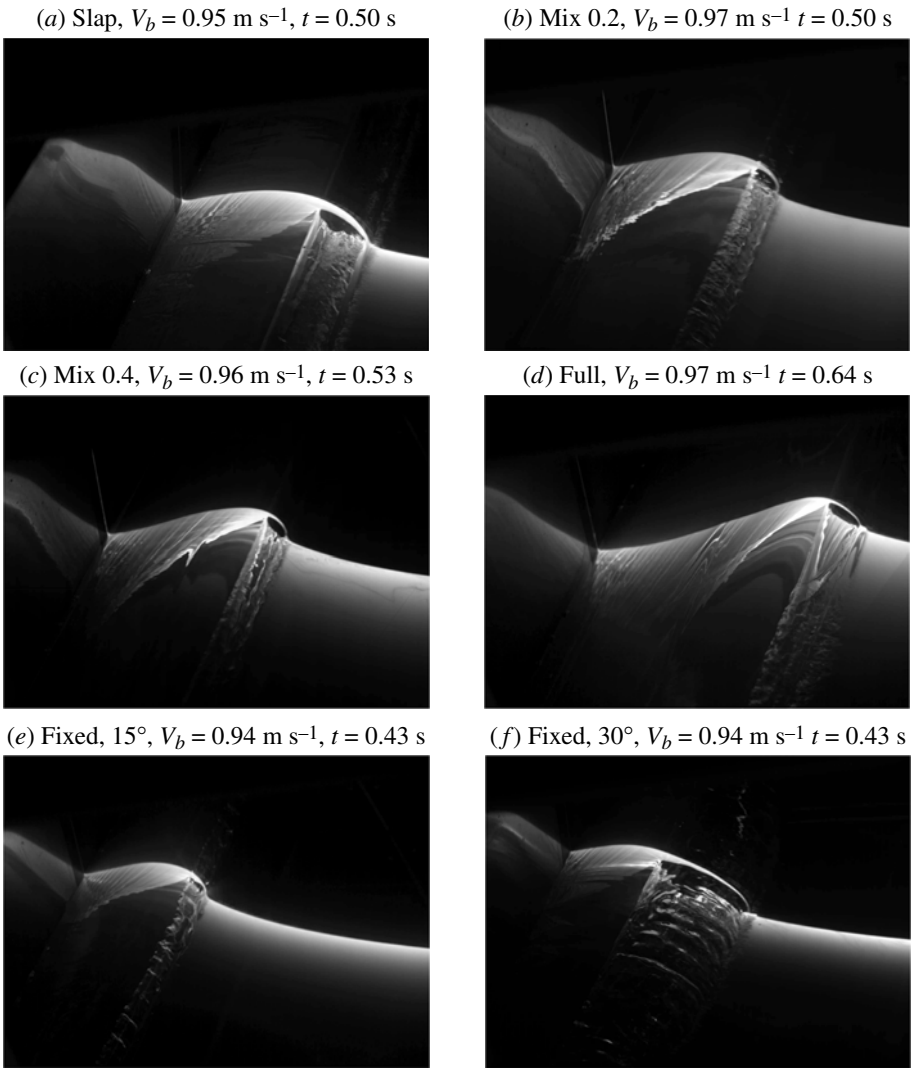

FIGURE 11. Wave images taken at the moment of plunging jet impact for different wave maker motion profiles. All cases were run at approximately the same wave board speed ($0.94 \leqslant V_b \leqslant 0.97$ m s^{-1}). The run condition and time after wave maker start for each image is as follows : (*a*) Slap, $Vb = 0.95$ m s^{-1}, $t = 0.50$ s; (*b*) Mix 0.2, $Vb = 0.97$ m s^{-1}, $t = 0.50$ s; (*c*) Mix 0.4, $Vb = 0.96$ m s^{-1}, $t = 0.53$ s; (*d*) Full, $Vb = 0.97$ m s^{-1}, $t = 0.64$ s; (*e*) Fixed, 15°, $Vb = 0.94$ m s^{-1}, $t = 0.43$ s; (*f*) Fixed, 30°, $Vb = 0.94$ m s^{-1}, $t = 0.43$ s.

impact point location relative to the wave board. In general, the Slap and Fixed cases tend to break sooner and closer to the wave board whereas the Full cases take longer to develop and break further from the wave board. The wave shapes observed in the Mix cases tend to be in between the Slap and Full cases. For the Fixed cases, the shape of the breaker is highly dependent on the angle of the wave board. Both Fixed cases were run at the same wave board speed but the greater board angle (30° versus 15° from vertical) throws the water much further away from the wave board and results in a longer, flatter plunging jet.

3.2. *Contact points*

In this section, measurements and analysis of the contact point heights are presented and discussed. This includes the trajectories of the contact point height versus time (§ 3.2.1), relationships between maximum contact point height and various wave maker parameters (§ 3.2.2), and analysis concerning the time at which the maximum contact point height occurs (§ 3.2.3).

3.2.1. *Contact point trajectories*

The height of the water surface contact point on the wave board, Z_c (relative to the undisturbed water level), for the various motion categories is plotted versus time in figure 12. Each of the six subplots contains data for most of the values of V_b used in each category. (Curves for several intermediate values of V_b were left out for clarity of presentation.) All of the contact point trajectories consist of an initial rise along the wave board leading to a maximum height, followed by a decline in height. This decline coincides with the generation of a wave crest that moves away from the wave board. At the lower speeds in all motion categories and at all speeds in the Full motion category, a secondary plateau occurs after Z_c reaches its peak but before it continues its fall to below zero.

Normalized contact point trajectory data from a representative set of cases encompassing the full range of board speeds for each motion category are plotted on a single graph of $Z_c/(Z_c)_{max}$ versus $t/(t_c)_{max}$ in figure 13(*a*), where $(Z_c)_{max}$ is the maximum contact point height in the curve for each experimental condition and $(t_c)_{max}$ is the time at which this maximum occurs. As can be seen in the figure, for $0.1 \lessapprox (t/(t_c)_{max} \leqslant 1$ all of the curves are nearly identical, indicating that a function of a single variable, $z_c' = f(t')$, where $(z_c', t') = (Z_c/(Z_c)_{max}, (t/(t_c)_{max})$, can be used to represent the data for all wave maker motions. The dashed line in the plot is a parabola constrained to go through the origin and have a maximum at $(z_c', t') = (1, 1)$. This parabolic, i.e. ballistic, trajectory $(z_c' = 2t' - t'^2)$ is clearly an excellent representation of the data in the range $0.1 \lessapprox t' \leqslant 1$. A ballistic trajectory of the contact line for streamwise positions between the stem and the first maximum was also suggested for three-dimensional ship bow flows on theoretical grounds by Noblesse *et al.* (2006). For $t' > 1.0$, the trajectories of the highest-Froude-number cases for the Slap and Fixed wave maker motion categories closely adhere to the ballistic trajectory throughout the motion, crossing $z_c' = 0$ at $t' \approx 2.0$. Other cases take longer to fall to $z_c' = 0$ with a secondary maximum of z_c' occurring for the lowest Froude numbers in the Full and Mix 0.4 cases. To characterize the time scale of the entire contact point trajectory, the same data are re-plotted in figure 13(*b*) with time normalized by the wave maker run time, t_{wm}. As can be seen from the plot, in the falling portions of the contact point trajectories for $z_c' < 0.6$ the curves for the various wave maker motions are nearly the same such that almost all cases cross $z_c' = 0$ at about $t/t_{wm} = 1.1$. There are three cases that return to $z_c' = 0$ later than the other trajectories. These three cases, which are the fastest Slap and Fixed cases, are the same cases that most closely follow the ballistic trajectory in figure 13(*a*).

3.2.2. *Maximum contact point height*

The relationship between the wave maker motions and the scaling parameter $(Z_c)_{max}$ is now examined. As can be seen in the plots in figure 12, the maximum contact point height, $(Z_c)_{max}$, which is often used as a measure of bow wave height in naval hydrodynamics studies, increases with increasing V_b in each motion category, and the time at which the maximum contact point height occurs, $(t_c)_{max}$, is approximately the same for all cases $((t_c)_{max}\sqrt{g/d} \approx 1.2)$. The dependence of $(Z_c)_{max}$ and $(t_c)_{max}$ on F_b

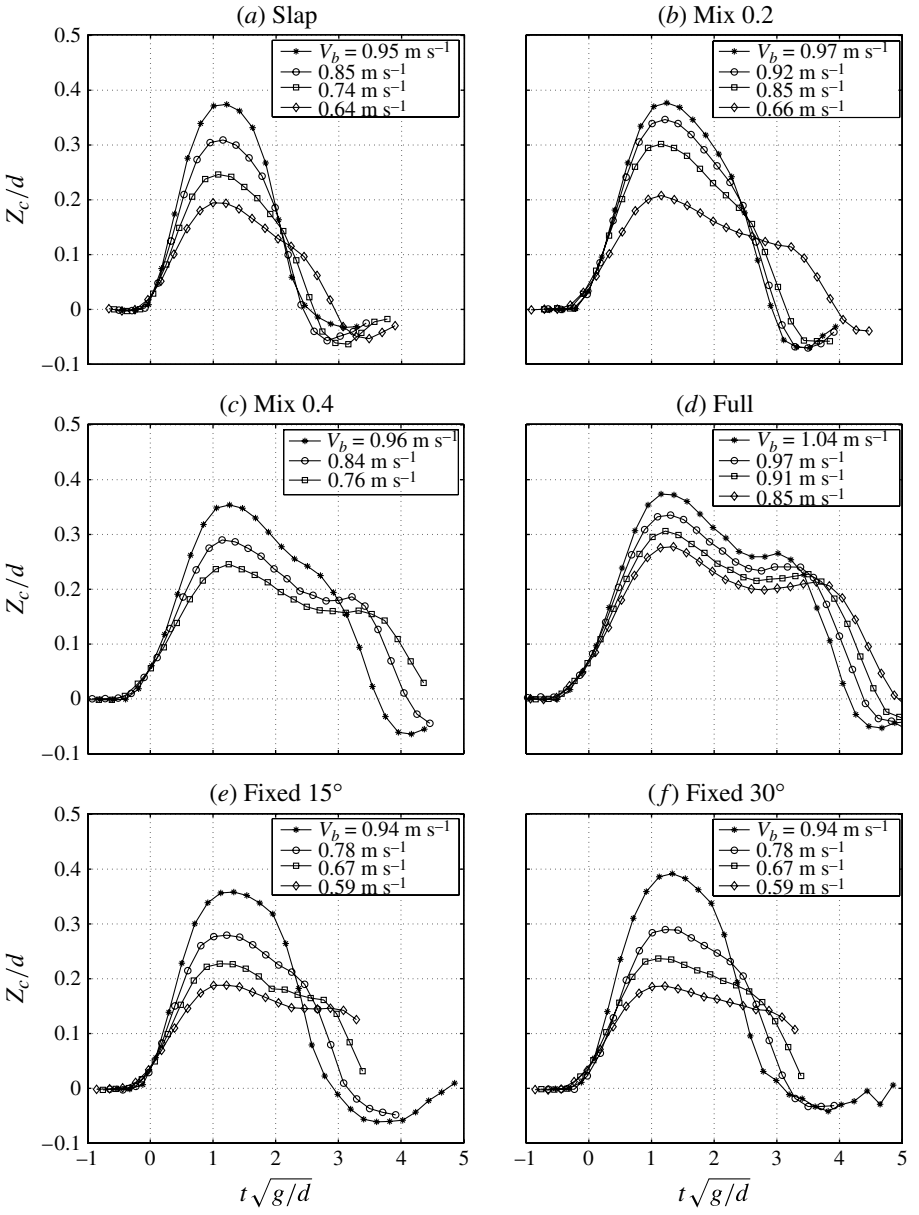

FIGURE 12. Plots of contact point height (normalized by draft) versus non-dimensional time $t\sqrt{g/d}$ for (*a*) Slap, (*b*) Mix 0.2, (*c*) Mix 0.4, (*d*) Full, (*e*) Fixed, $\theta = 15°$ and (*f*) Fixed, $\theta = 30°$. Each curve is the average of three runs. For the sake of visual clarity, the data for several wave maker speeds intermediate to those plotted here are not shown.

are examined in figures 14 and 15, respectively. As can be seen in figure 14, $(Z_c)_{max}/d$ varies nearly linearly with F_b, even though the wave shapes vary widely from one wave maker motion category to another at approximately the same F_b, see figure 11. The straight line is a least squares fit to the data and is given by

$$(Z_c)_{max}/d = 1.432F_b - 0.104. \tag{3.1}$$

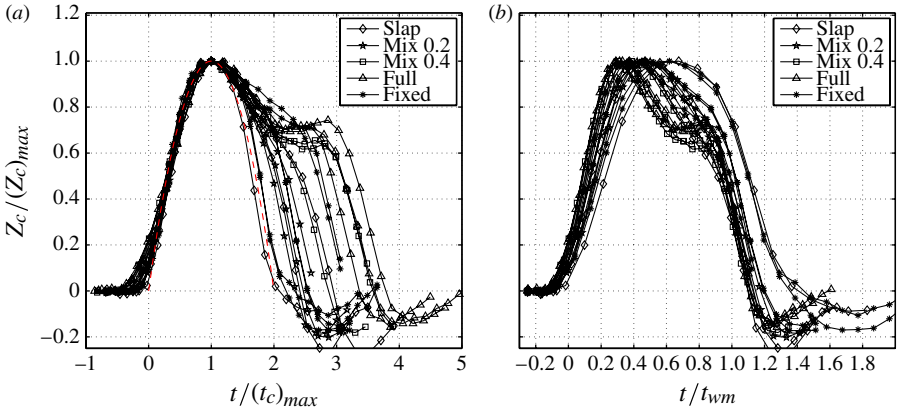

FIGURE 13. (Colour online available at journals.cambridge.org/flm) Non-dimensional contact point height, $z_c' = Z_c/(Z_c)_{max}$, versus non-dimensional time. In (*a*), time is normalized by $(t_c)_{max}$, where $(t_c)_{max}$ is the time that Z_c reaches its maximum, and in (*b*), time is normalized by t_{wm}, where t_{wm} is the wave maker motion time. The dashed curve in (*a*) is a parabola constrained to go through (0, 0) and have a maximum at (1, 1), i.e. $z_c' = 2t' - t'^2$.

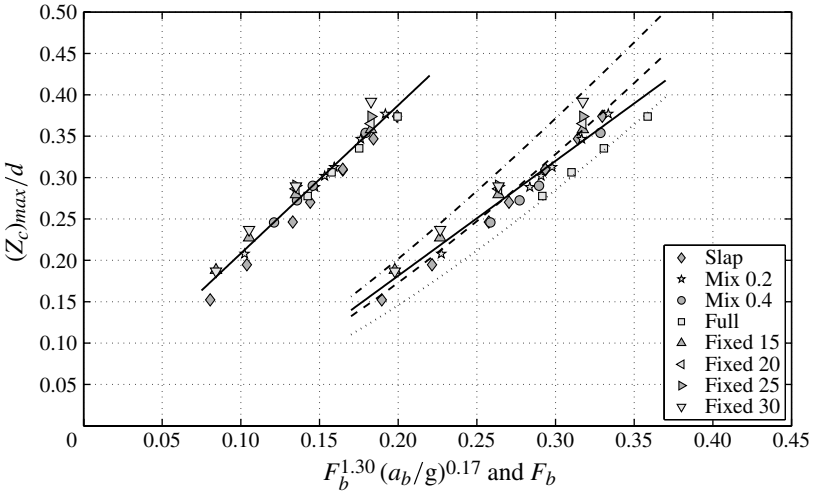

FIGURE 14. Non-dimensional maximum contact point heights, $(Z_c)_{max}/d$, versus $F_b^{1.30}a_b^{0.17}$ in the left-hand group of data points and versus F_b in the right-hand group of data points. The solid straight lines are least squares fits to the two groups of data: $(Z_c)_{max}/d = 1.859F_b^{1.30}a_b^{0.17} + 0.024$ and $(Z_c)_{max}/d = 1.432F_b - 0.104$. The other lines are (3.5) with $\alpha_E = 14.0°$ (– · –), 18.6° (– – –) and 25.0° (· · ·).

The root-mean-square (r.m.s.) error of the $(Z_c)_{max}/d$ values about this line is ±0.016, which is about 5.5 % of the average of all of the data. A linear relationship between $(Z_c)_{max}/d$ and F_b was also observed in previous 2D+T studies (Shakeri *et al.* 2009*a*,*b*) where the wave maker used a single motion profile over a wide range of wave board speeds. The possibility that $(Z_c)_{max}/d$ depends on both F_b and the wave board

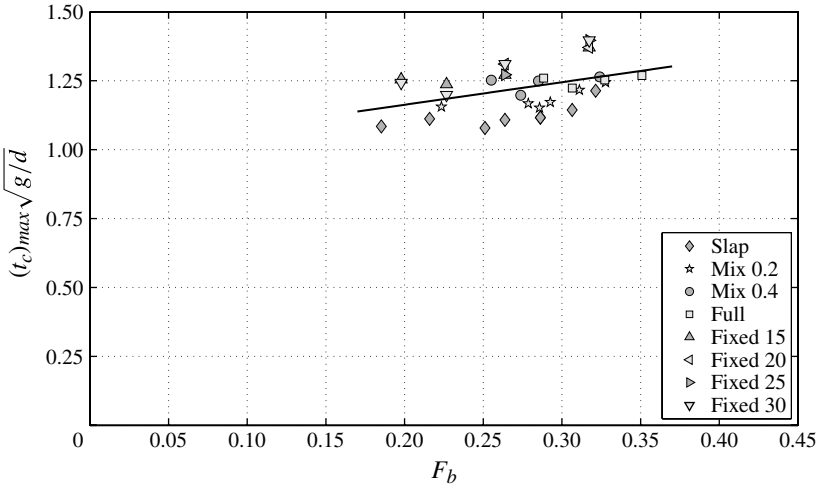

FIGURE 15. Non-dimensional time to maximum contact point height, $(t_c)_{max}\sqrt{g/d}$, versus F_b. The straight line, $(t_c)_{max}\sqrt{g/d} = 0.818F_b + 0.999$, is a least squares fit to the data. The average of the $t_c max\sqrt{g/d}$ values is 1.23.

acceleration, a_b, was also explored. To this end, the function

$$(Z_c)_{max}/d = A_1 F_b^{A_2} a_b^{A_3} + A_4 \tag{3.2}$$

was fit to the data, resulting in best-fit values of $A_1 = 1.859$, $A_2 = 1.30$, $A_3 = 0.17$ and $A_4 = 0.024$. Note the low value of A_3 relative to A_2, suggesting significantly greater dependence on wave speed than acceleration. The data on the left in figure 14 is plotted versus $F_b^{1.30} a_b^{0.17}$ and, as can be seen from the figure, some decrease in scatter about the fitted straight line is achieved (the r.m.s. error is ± 0.010 or 3.5 % of the average of all of the data).

Using theory and experimental data, Noblesse *et al.* (2006, 2008*a*) found that the relationship between $(Z_c)_{max}/d$, the ship model Froude number $F = U/\sqrt{gd}$, where U is the forward speed of the model, and the entrance angle of the bow, $2\alpha_E$, could be approximated by

$$\frac{(Z_c)_{max}}{d} = 2.2\frac{F^2}{1+F}\frac{\tan\alpha_E}{\cos\alpha_E}. \tag{3.3}$$

This relationship was shown to have relatively good agreement with data from experiments using wedge-shaped hulls with half-entrance angles ranging from 5 to 26°, though some scatter exists in the data. Using the 2D + T approximation,

$$U_b = \tan\alpha_E U, \tag{3.4}$$

this expression becomes

$$\frac{(Z_c)_{max}}{d} = \frac{2.2}{\cos\alpha_E}\frac{F_b^2}{(\tan\alpha_E + F_b)}. \tag{3.5}$$

Thus, an entrance angle must be selected to compare (3.3) to the present data. However, in the 2D + T approximation, unless α_E is determined by simulating a specific hull form, a given wave board speed can correspond to a variety of α_E-U combinations, see (3.4). Since there is no corresponding three-dimensional hull form

in the present work, a least squares fit of (3.5) to the present data was performed and resulted in a value of $\alpha_E = 18.6°$. Curves of equation (3.5) for $\alpha_E = 14$, 18.6 and 25° are plotted in figure 14 to compare with the present data. As can be seen from the plot, the curves for $\alpha_E = 14$ and 25° nicely bracket the data and the curve for $\alpha_E = 18.6°$ is quite close to the above-discussed linear fit to the data, equation (3.1). Interestingly, this range of entrance angles is similar to that of the ship-models utilized to obtain the experimental data (5–26°) that was used by Noblesse *et al.* (2006, 2008*a*) to determine the value of the coefficient in (3.3).

3.2.3. *Time to maximum contact point height*

The relationship between the wave maker motions and the scaling parameter $(t_c)_{max}$ is now examined. The non-dimensional time to the maximum contact point height, $(t_c)_{max}\sqrt{g/d}$, is plotted versus F_b in figure 15. The values of $(t_c)_{max}\sqrt{g/d}$ are relatively constant and have an average of 1.23, a range of 1.08–1.40 and an r.m.s. error of ±0.077 (±6.3 % of the average). The straight line in the plot ($(t_c)_{max}\sqrt{g/d} = 0.818F_b + 0.999$) is a least squares fit to the data and indicates a rather weak dependence on F_b. The relatively small range of $(t_c)_{max}\sqrt{g/d}$ values (about 26 % of the average) should be compared with the much larger range of total wave maker run times (0.54 s $\leqslant t_{wm} \leqslant$ 1.35 s, about 86 % of the mean value) in this study.

Values of $(t_c)_{max}\sqrt{g/d}$ were also determined in 2D + T studies simulating the 5415 hull form (Shakeri *et al.* 2009*a*) and the Athena hull form (Shakeri *et al.* 2009*b*). For the experiments with the 5415 hull form, the model draft was $d = 0.91$ m and the total water depth was $H = 1.83$ m. Over the model speeds used in the study, the values of $(t_c)_{max}$ were nearly constant with an average of $(t_c)_{max}\sqrt{g/d} = 1.80$ and a range of 0.262. For the experiments with the Athena hull form, $d = 0.62$ m and $H = 1.53$ m. In this case, the values of $(t_c)_{max}$ were again nearly constant, with an average of $(t_c)_{max}\sqrt{g/d} = 1.43$ and range of 0.08. Thus, although the average dimensionless times from the present and previous studies vary relative to each other, they are nearly constant within each study.

Using the 2D + T transformation, $x = Ut$, and taking the average value of the measured $(t_c)_{max}\sqrt{g/d}$ data, one finds that the streamwise position of the maximum contact point height along an equivalent three-dimensional model increases linearly with U:

$$x_{max} = 1.23U\sqrt{d/g}. \tag{3.6}$$

(Use of the average value of $t_c max\sqrt{g/d}$ in the above relationship is justified since the straight line that was fit to the data varies by only about 9 % of the average value over the range of F_b used herein.) Using fundamental theoretical considerations and experimental measurements, Noblesse *et al.* (2006, 2008*a*) calculated the position of the crest in the contact line profile on ship forms with wedge-shaped bows and found that for high Froude numbers:

$$X_b = 1.1\cos^7(\alpha_E)U\sqrt{d/g}, \tag{3.7}$$

where X_b is the distance from the stem to the crest (see (7.1) in Noblesse *et al.* (2008*a*) where T_b is used in place of X_b as used herein). In the limit of small α_E, this relationship is in good agreement with the present experimental results. Similar results were also found in the above-mentioned calculations of Ogilvie (1972) and Calisal & Chan (1989).

In Noblesse *et al.* (2009) the effects of rake and flare on the wedge-shaped bow results were examined numerically using a thin-ship approximation. Rake is

Motion	Equivalent φ
Slap	1.0
Mix 0.2	0.55
Mix 0.4	0.38
Full	0.29
Fixed	0

TABLE 2. Equivalent values of φ, as defined in Noblesse *et al.* (2009), for the motion categories in the present study.

characterized by the angle δ of the stem line relative to vertical and the bow flare is characterized by a parameter φ given by

$$\varphi = \frac{\tan\alpha - \tan\alpha'}{\tan\alpha + \tan\alpha'} \tag{3.8}$$

where 2α is the entrance angle at the mean waterline and $2\alpha'$ is the entrance angle at the keel depth. For example, for wedge shaped bows with vertical walls, $\delta = 0$ and $\alpha = \alpha' = \alpha_E$, so $\varphi = 0$ as well. The Slap, Mix and Full wave maker motion categories correspond to three-dimensional hull shapes with a vertical ship stem, $\delta = 0$. Also, using L_m as an effective streamwise length of the bow region, $\tan\alpha \approx B_w/L_m$ and $\tan\alpha' \approx B_k/L_m$. When these expressions are plugged into (3.8), L_m cancels out and φ is dependent only on B_w and B_k. The equivalent values of φ for the wave maker motion categories are listed in table 2. The Fixed motion categories are anomalous in regards to δ and φ. For these cases, $\alpha = \alpha'$ and (3.8) yields $\varphi = 0$. However, the wave board is tilted from vertical at $t = 0$, producing an equivalent three-dimensional hull shape with no stem. A realistic three-dimensional hull for the case of $\varphi = 0$ would include a stem with a forward leaning rake angle $\delta > 0$. Noblesse *et al.* (2009) predict that with zero rake, variations of φ over the range corresponding to the present study produce variations of $(Z_c)_{max}$ (called Z_b in their paper) and $U\,(t_c)_{max}$ (called T_b in their paper) from the wedge-shaped bow results, (3.3) and (3.7), respectively, of about 20 % (see Noblesse *et al.* 2009, figure 25), in approximate agreement with the ranges found in the present study in the Slap, Mix and Full wave maker motions, see figures 14 and 15.

3.3. *Wave crests*

In this section, we present and discuss the measurements of the wave crest height and the wave crest speed. In the early stages of the wave development, the maximum water surface height (Z_p) is coincident with the contact point. Later, after the wave crest moves away from the wave board, Z_p is typically located at the wave crest. At later times in many plunging jet cases, Z_p may be located on the splash generated in front of the plunging jet impact site; however, in the present data the splash portion of the profile was not considered when measuring Z_p. Examples of the temporal history for the normalized maximum water surface height (Z_p/d) for six wave maker motions with approximately the same wave board speed ($V_b \approx 0.96$ m s^{-1}) are plotted in figure 16. The photographs in figure 11 were taken from these same six cases. As mentioned above, from the initial rise to nearly the maximum height, these curves are identical to their corresponding contact point trajectories. The Slap, Mix 0.2, Mix 0.4 and Full are shown together in figure 16(*a*). In the Slap case, Z_p/d has a pronounced maximum at about the time of the maximum contact point height and then a steady descent which

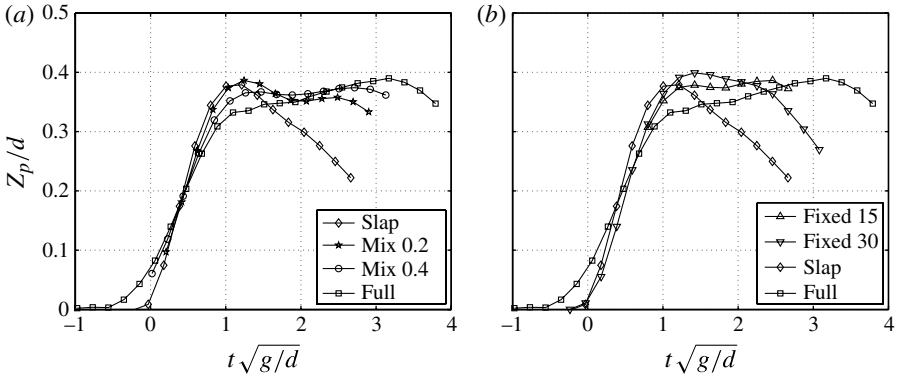

FIGURE 16. Non-dimensional maximum surface height (Z_p/d) versus non-dimensional time ($t\sqrt{g/d}$) for various wave maker motion profiles, all at approximately $V_b = 0.96$ m s^{-1}. For clarity, all of the rotating cases (Slap, Mix and Full) are shown together in (*a*) and the Fixed 15 and Fixed 30 cases are shown with the Slap and Full cases in (*b*).

occurs more slowly than the corresponding descent of Z_c/d, see figure 12(*a*). From the movies of this Slap case, it can be seen that during this decrease Z_p is located on the wave crest as the wave is breaking. In the Full case, on the other hand, Z_p/d continues to rise slowly after the time of the maximum contact point height prior to breaking. The Mix 0.2 and Mix 0.4 cases show a steady progression in curve shape toward the Full case. As can be seen in table 1, the Mix 0.2, Mix 0.4 and Full cases also have a steady progression in total wave board translation. The Fixed cases with wave board angles of 15 and 30° are compared with the Slap and Full cases in figure 16(*b*). The Fixed cases both have higher maximum values and do not seem to follow the patterns of either the Slap or the Full cases. It should be noted that the Fixed cases tend to break early and close to the wave board and thus often do not have a clear wave crest as it is typically defined (recall figures 11(*e* and *f*)).

The non-dimensional maximum water surface height for each experimental condition, $(Z_p)_{max}/d$ (the maximum values in curves like those shown in figure 16), are plotted versus F_b in figure 17. Similar to the behaviour of the maximum contact point height (figure 14), $(Z_p)_{max}/d$ varies nearly linearly with F_b. The straight line in the figure, $(Z_p)_{max}/d = 1.345F_b - 0.054$, is a least squares fit to the data. The r.m.s. error about this line is ± 0.014 (4.4 % of the average of all of the data) and is similar to that found for the maximum contact point heights. A linear relationship between $(Z_p)_{max}/d$ and F_b was also observed in previous 2D + T studies (Shakeri *et al.* 2009*a*,*b*) where the wave maker used a single motion profile over a wide range of wave board speeds.

Wave crest speed was determined from the trajectories of the horizontal position of the wave crest from the time the wave detached and moved away from the wave board until it disappeared later in the breaking process. The horizontal position of the wave crest was found to increase nearly linearly with time so the phase speeds were determined by least squares fit of straight lines to the data. The normalized wave crest speed (V_{crest}/V_b) versus F_b is plotted in figure 18. The values generally decrease from 2.6 to 2.0 as F_b increases. Measurements from simulations of the 5415 hull form (Shakeri *et al.* 2009*a*) are also plotted in this figure. For those measurements, values of V_{crest}/V_b also decrease with increasing F_b and for the range of F_b in the present measurements, $0.18 \leqslant F_b \leqslant 0.36$, fall at the lower part of the range of the present data.

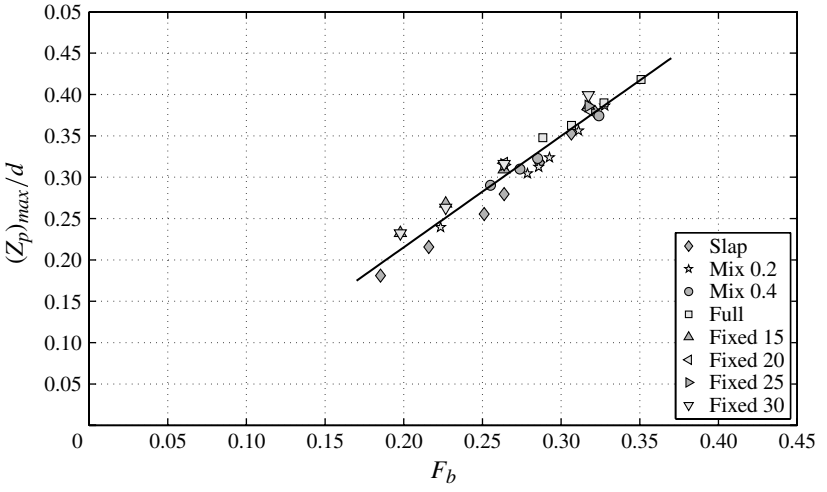

FIGURE 17. Non-dimensional maximum surface heights ($(Z_p)_{max}/d$) versus F_b. The straight line, $(Z_p)_{max}/d = 1.345F_b - 0.054$, is a least squares fit to the data.

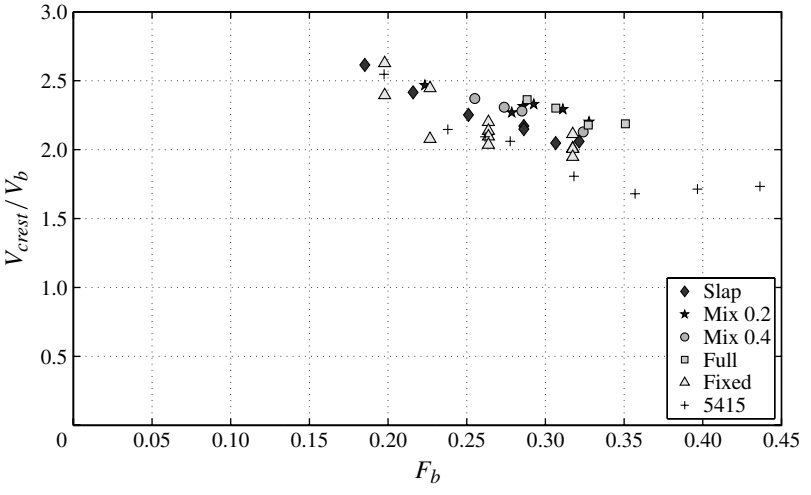

FIGURE 18. Normalized wave crest speed versus F_b for all wave maker motion categories. Data from Shakeri *et al.* (2009*a*) are included.

For $F_b \geqslant 0.36$, V_{crest}/V_b values from Shakeri *et al.* (2009*a*) are approximately constant, $V_{crest}/V_b = 1.7$.

3.4. *Effect of wave board acceleration*

As discussed in § 2.3, the average wave board acceleration, a_b, is inversely proportional to the rounding period parameter T_R (see (2.2)) and for all of the data discussed up to this point, $T_R = 0.5$. However, in order to investigate the effects of a_b as an independent variable, several experiments were performed with $T_R = 0.4$ and $T_R = 0.6$. Modifying T_R in this way results in acceleration values of $1.25a_b^*$ and $0.83a_b^*$, respectively, where a_b^* represents a_b with $T_R = 0.5$. Three sets of experiments

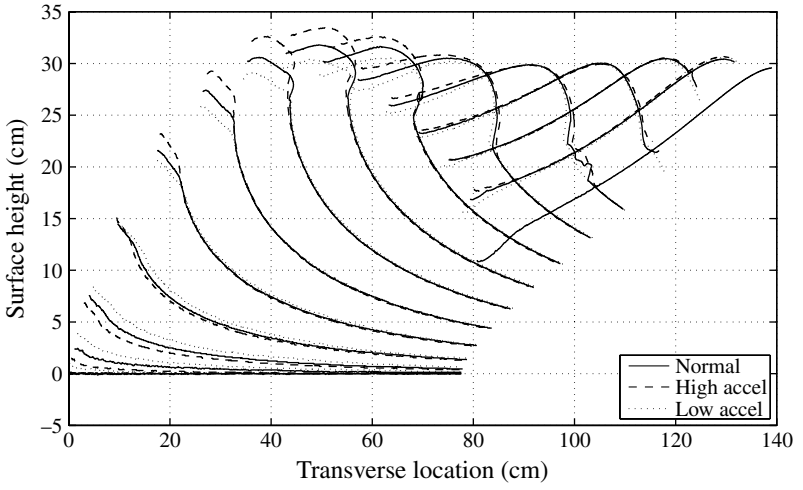

FIGURE 19. Wave profiles for Mix 0.2, $V_b = 0.92$ m s^{-1} (constant), run with three different board accelerations ($a_b = V_b/T_R t_{wm}$) corresponding to 'Normal' ($T_R = 0.5$), 'High accel' ($T_R = 0.4$) and 'Low accel' ($T_R = 0.6$). Surface profiles are plotted at the same 1/16 s intervals.

were performed with these varied accelerations and single values of V_b: Slap with $V_b = 0.85$ m s^{-1}, Mix 0.2 with $V_b = 0.92$ m s^{-1} and Mix 0.4 with $V_b = 0.96$ m s^{-1}. Water surface profiles for the Mix 0.2 case using all three accelerations are shown in figure 19. The time interval between profiles is 1/16 s. As can be seen from the plot, profiles from the different acceleration schemes deviate during the early stages of the wave board motion but then appear to converge after the wave has detached from the wave board. This is further illustrated by the plots of Z_c/d versus $t\sqrt{g/d}$ and Z_p/d versus $t\sqrt{g/d}$ given in figures 20(*a*) and 20(*b*), respectively. Data is given for the Mix 0.2 case and the three values of a_b. In both plots, the three curves are only divergent in the region of maximum surface height. This behaviour was observed in the other two cases that were tested with varied acceleration. Plots of the normalized maximum contact point height ($(z_c/d)_{max}$) versus a_b for the three wave-board motions are shown in figure 21. All three cases show a similar moderate increase in maximum contact point height with increased wave board acceleration. Thus, wave board acceleration appears to have a mild influence on both the maximum contact point height and the maximum water surface height, but at later times, when the wave has detached from the wave board, a_b has little effect on the wave height.

3.5. *Breaker details*

In this section, we present and discuss the results describing the breaker type and shape of the wave crest at the moment of incipient breaking. The data from figure 17 are replotted in figure 22 with each data point marked according to breaker type. Most of the breakers are characterized as either spillers or plungers, while one of the breakers was deemed to be transitional between the two main types. As can be seen from the plot, regardless of wave maker motion category, only spilling breakers occur when $F_b < 0.26$ and only plunging breakers occur when $F_b > 0.29$, while both types of breakers occur in the small overlap region $0.26 < F_b < 0.29$. By comparing figure 22 with figure 17, it can be seen that each region of breaker type contains the entire set of wave maker motion categories. Thus, F_b is a primary determiner of breaker type.

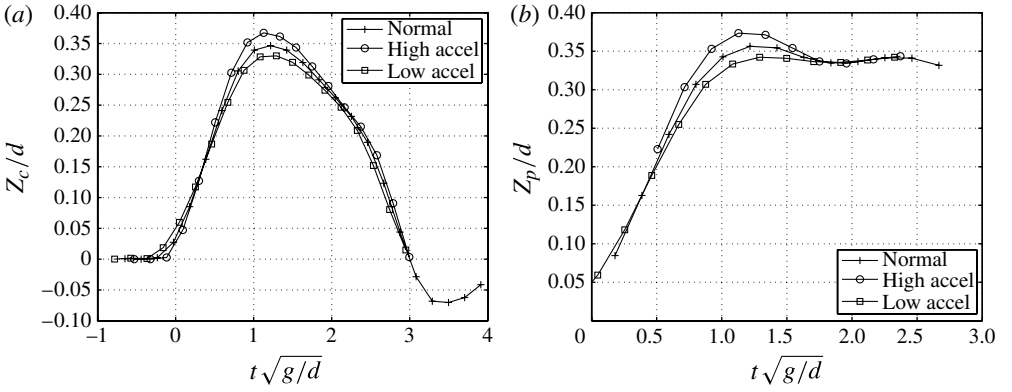

FIGURE 20. Effect of wave board acceleration for Mix 0.2, $V_b = 0.92$ m s^{-1}. (*a*) Non-dimensional contact point heights and (*b*) non-dimensional maximum surface heights, both plotted against normalized time. Three different board accelerations are used including 'Normal' ($T_R = 0.5$), 'High accel' ($T_R = 0.4$) and 'Low accel' ($T_R = 0.6$).

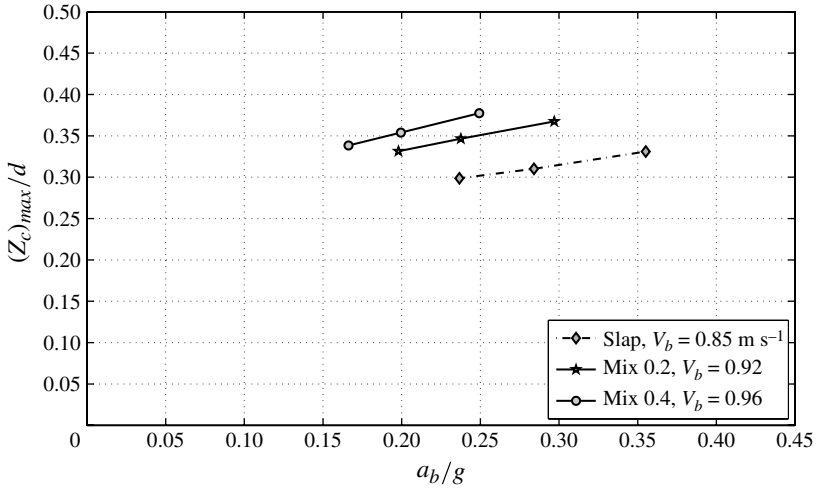

FIGURE 21. Maximum contact point heights versus normalized wave board acceleration for cases with varied wave board acceleration parameters. Rounding period (T_R) values of 0.4, 0.5 and 0.6 are used to vary board acceleration.

Up to this point, it has been shown that several parameters describing the gross characteristics of the wave (contact point height, time of the maximum contact point height, maximum water surface height, wave phase speed and breaker type) show a primary dependence on the wave board Froude number, F_b, with little differentiation among the various wave maker motion categories. However, from the photographs in figure 11, it can be seen that the wave crest shape at the moment of plunging jet impact varies dramatically with the wave maker motion category for waves generated at nearly the same F_b. To explore these variations quantitatively, several geometric characteristics describing the crest shape at the moment of jet impact in the plunging breakers and the moment of transition to turbulent flow in the strongest spilling breakers were examined. These characteristics are defined on a photograph of the

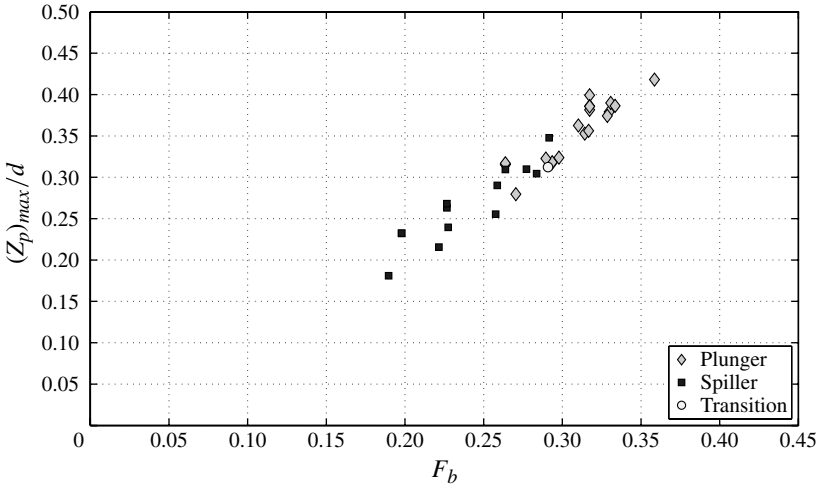

FIGURE 22. Identification of breaker type on a plot of non-dimensional maximum surface heights ($(Z_p)_{max}/d$) versus F_b for all wave maker motion profiles. The data points are the same as those in figure 17.

crest of a plunging breaker in figure 23. The profiles of the crests of the strong spilling breakers look nearly identical to the plunging breakers. The profile location corresponding to the impact point in the plunging breaker is called the toe point in the strong spilling breakers. Two geometric characteristics were measured from the profiles: the horizontal breaking-region length, L_{br}, defined as the horizontal distance from the wave crest to the jet impact point in the plunging breakers or the toe point in the spilling breakers; and the breaking-region height, H_{br}, defined as the vertical distance from the jet impact point or toe point to the wave crest.

A plot of L_{br}/d versus F_b is given in figure 24(a). As can be seen in the figure, there is a wide variation of L_{br}/d (from about 0.01 to 0.2) over the various breakers and there is little functional relationship with F_b in contrast to the gross wave characteristics discussed above, see for example figure 14. In view of this finding, the behaviour of L_{br}/d versus a number of other wave maker motion parameters was explored. The best correlation was found with L_{br}/d versus the dimensionless wave board acceleration, a_b/g, as shown in figure 24(b). The data from the Slap, Mix and Full cases show a monotonically increasing L_{br}/d with wave board acceleration with the data falling on approximately the same straight line. The solid line given in the figure, $L_{br}/d = 0.614(a_b/g) - 0.061$, is a least squares fit to the Slap, Mix and Full data and the r.m.s. error is ± 0.010. For the Fixed cases, the values of L_{br}/d also increase with a_b/g, but with an additional dependence on the wave board angle, α. Larger values of α result in sometimes dramatically larger rates of increase of L_{br}/d with a_b/g. Values of L_{br}/d were also measured for the runs with varied a_b and constant F_b (recall § 3.4). This data is plotted in figure 25 along with the Slap, Mix and Full data from figure 24(b). As can be seen in the figure, the data with varied acceleration follow the same trend as the original data, thus confirming the very strong linear dependence of L_{br}/d on a_b/g.

A plot of H_{br}/d versus a_b/g is given in figure 26. The solid straight line, $H_{br}/d = 0.503(a_b/g) - 0.037$, is a least squares fit to the data for the Slap, Mix and Full cases (the r.m.s. error is ± 0.016). Although there is a monotonic increase in

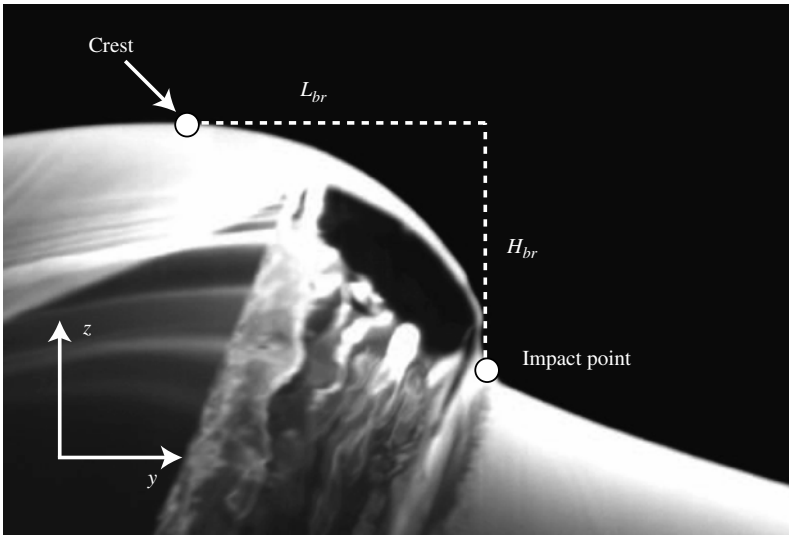

FIGURE 23. Geometric characteristics of the crest profile of a typical plunging breaker. The profile of a strong spilling breaker is qualitatively similar; however, in strong spilling breakers, the profile point corresponding to the impact point in the above image is called the toe point.

H_{br}/d with increasing a_b/g in all of the data, there is significantly more scatter about the fitted line than there was in the plot of L_{br}/d versus a_b/g in figure 24(*b*). The slope of the breaking region, $S_{br} = H_{br}/L_{br}$, is plotted versus a_b/g in figure 27. No clear relationship between S_{br} and a_b/g is apparent from the data; however, there does appear to be a demarcation between the various wave maker motion categories around $S_{br} \approx 1$. The S_{br} values for the Slap and Mix 0.2 cases are all less than 1.02. On the other hand, the Mix 0.4 and Full cases, with the exception of two strong spillers, all have S_{br} values greater than 1.18. Thus, it appears that the Slap and Mix 0.2 wave maker motion categories produce more horizontally oriented jets than the Mix 0.4 and Full motion categories, whose jets tend to be more vertical. The S_{br} values for the Fixed cases cover a wide range, similar to the corresponding L_{br} values shown in figure 24(*b*).

4. Conclusions

Waves generated by a novel programmable two-dimensional wave maker with a flexible wave board were studied. The wave maker motions consisted of combinations of two fundamental motions of a flat plate: translation at a fixed angle (called Fixed wave maker motions) and rotation about a point that is either stationary (called Slap) or moving (called Mix and Full). In all of the wave maker motions, the wave board accelerates, moves at constant speed and/or rate of rotation for a period of time and then decelerates to zero speed. Through the 2D + T approximation, these motions simulate a series of three-dimensional model ship bows with parametrically varying shape. The cinematic LIF wave-measurement technique employed in these experiments was used to measure the sequence of shapes of the resulting waves with high spatial and temporal resolution. The experiments are used to explore the relationships between the bow shape parameters and various physical characteristics of the resulting waves. The experimental application of the 2D + T technique combined with the cinematic

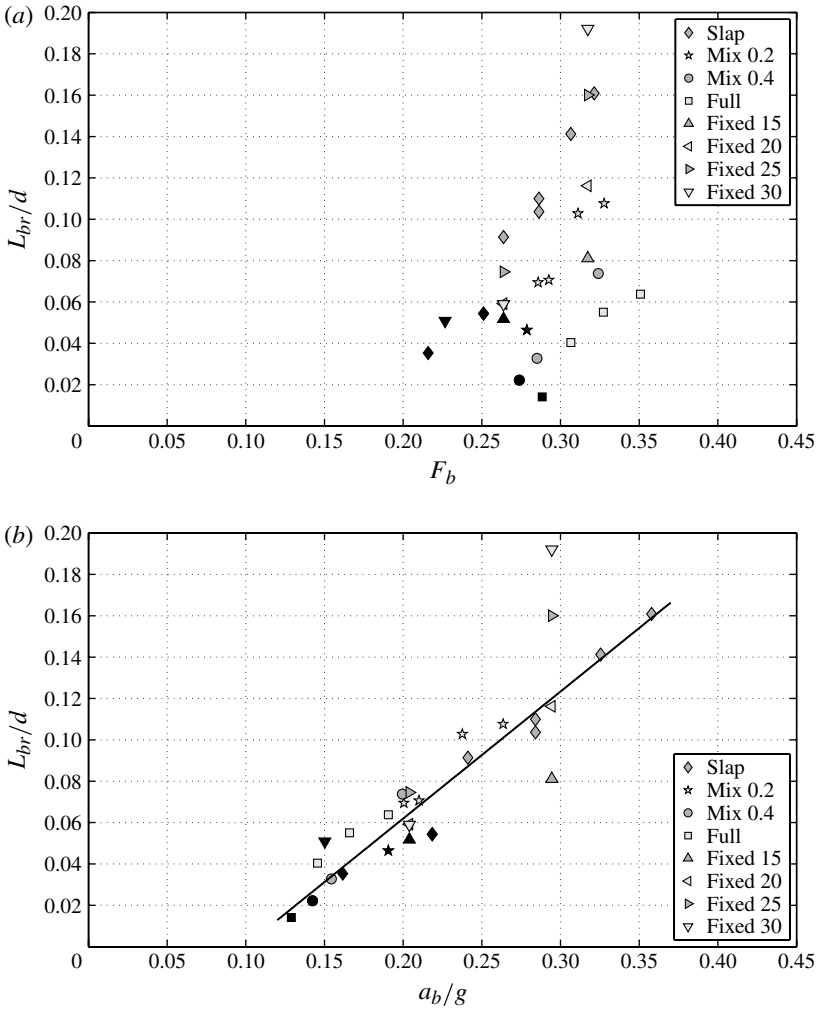

FIGURE 24. Normalized breaking-region horizontal length, L_{br}/d, versus (*a*) F_b and (*b*) a_b/g. The symbols filled with black correspond to strong spilling breakers while the other symbols correspond to plunging breakers. The straight line in (*b*), $L_{br}/d = 0.614(a_b/g) - 0.061$, is a least squares fit to the data for the Slap, Mix and Full cases.

LIF wave measurements allowed for a series of high-resolution wave measurements for a total of 46 bow shapes with a keel depth of 0.892 m. The 2D + T approach neglects flow characteristics such as the hull boundary layer, the stagnation point at the stem and transverse waves, thus it is not claimed that this technique simulates a specific hull as accurately as experiments with three-dimensional models. However, the detail of the wave measurements including plunging jet shapes, the large number of bow shapes and the large scale of the equivalent three-dimensional ship models would be difficult to achieve individually, and would be exceptionally difficult to achieve in combination, in ship model basin experiments.

Analysis of the plots of contact point height (Z_c) versus time (t), indicates that there is a universal ballistic trajectory between the beginning of the wave maker motion and the time of the maximum contact point height while the total length of time that Z_c

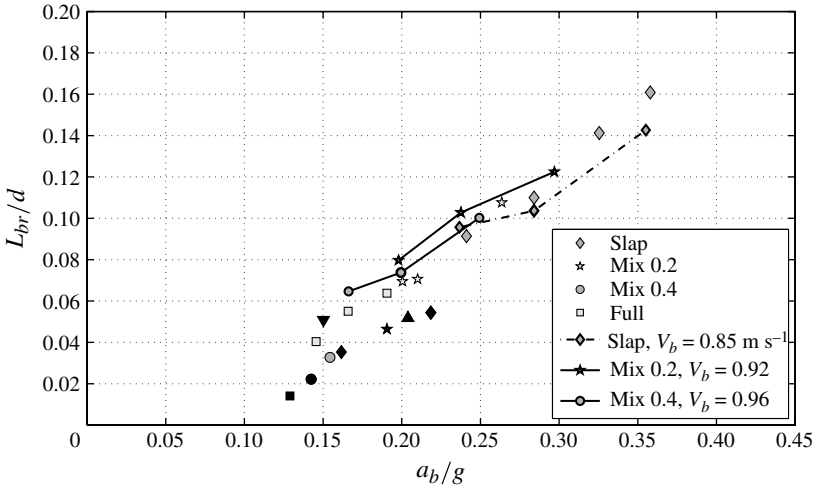

FIGURE 25. Normalized breaking-region horizontal length, L_{br}/d, versus a_b/g for the Slap, Mix 0.2 and Mix 0.4 cases with constant Froude number and varying a_b (lines) overlaying data points from figure 24. For clarity of presentation, the Fixed data has been omitted. The symbols filled with black correspond to strong spilling breakers while the other symbols correspond to plunging breakers.

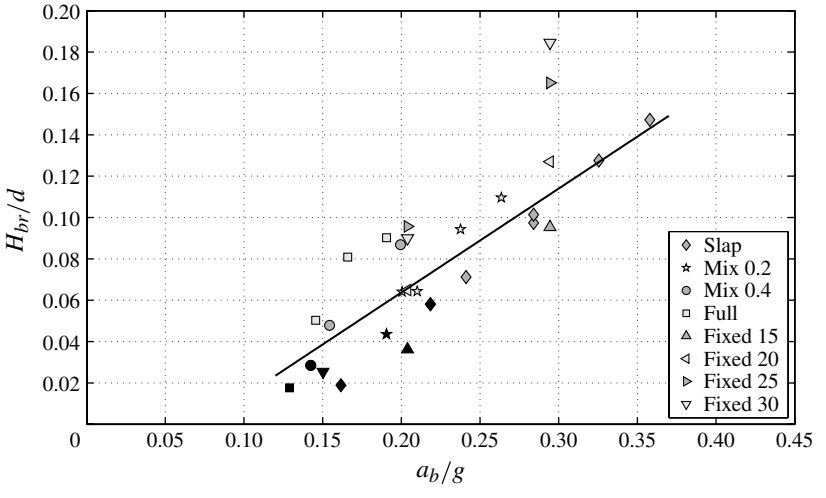

FIGURE 26. Normalized breaking-region height, H_{br}/d, versus a_b/g. The solid straight line, $H_{br}/d = 0.503(a_b/g) - 0.037$, is a least squares fit to the data for the Slap, Mix and Full cases. The symbols filled with black correspond to strong spilling breakers while the other symbols correspond to plunging breakers.

remains above the mean water level scales primarily with the wave maker run time, t_{wm}. The ballistic trajectory is given by $z_c' = 2t' - t'^2$ where $z_c' = Z_c/(Z_c)_{max}$, $(Z_c)_{max}$ is the maximum contact point height, $t' = t/(t_c)_{max}$ and $(t_c)_{max}$ is the time at which $(Z_c)_{max}$ occurs. It is found that $(Z_c)_{max}$ is primarily a linear function of the wave board Froude number, F_b, with effects introduced in the various wave maker motion categories (wave board slope, acceleration, etc.) contributing variations on the order

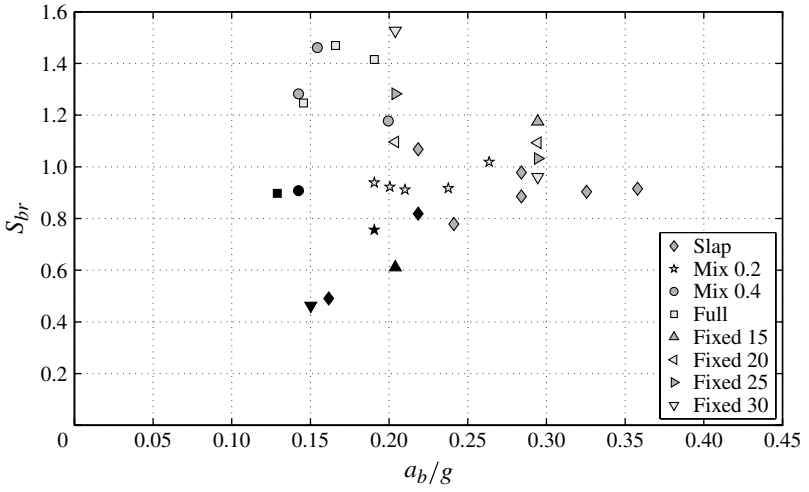

FIGURE 27. Breaking-region slope, S_{br}, versus wave board acceleration. The symbols filled with black correspond to strong spilling breakers while the other symbols correspond to plunging breakers.

of $\pm 10\,\%$ from the values determined from F_b alone. The values of $(t_c)_{max}$, however, depend only weakly on F_b with the total range of values being about $26\,\%$ of the mean, while the total percentage variation of the wave maker run time is about three times larger. In all cases, $(Z_c)_{max}$ occurs after the initial acceleration phase is finished and the wave board is moving at constant velocity. The maximum wave height and, to a lesser degree, the wave phase speed also show a primary dependence on F_b. The results presented here are in qualitative agreement with the work of Noblesse *et al.* (2006, 2008*a*,*b*, 2009, 2011) who showed, using simple theory and thin-ship calculations, that the contact point height is primarily a function of ship Froude number, which is typically based on ship forward speed and draft. The wave board Froude number and the ship Froude number can be shown to be proportional for an assumed or given bow entrance angle. The 2D + T results appear to agree with the results of Noblesse *et al.* for half-entrance angles approximately between 14° and 25°.

Photographs of breakers generated at about the same value of F_b but with different wave maker motion categories show that while these waves have approximately the same heights, phase speeds, etc., the crest shape at the time of jet impact in the plunging breakers, or the transition to turbulent flow in the spilling breakers, varies dramatically from one wave maker motion category to another. It was found that the plunging jet length and height scale much better with the wave board acceleration, a_b, than with the wave board Froude number. The wave board acceleration is believed to be related to the flow field and streamline pattern in the vicinity of the stem of the three-dimensional ship model, all of which is determined in a complex way by the stem shape and the model's forward speed.

The linear relationship between wave height and F_b observed in this study and the 2D + T relationship between ship speed, U, and wave board speed, $V_b \approx \alpha U$, suggests that a ship with a bow with a small entrance angle, α, moving at a particular forward speed would produce similar bow wave heights to a ship with a larger entrance angle moving at slower speed if the two cases had similar equivalent values of F_b. (This idea is implicit in the results of previous research, see for example, Ogilvie 1972 and

Noblesse *et al.* 2006.) The flow field around the bow and the rise of water upstream of the stem would be different for the two cases and the resulting variations in lateral acceleration of the fluid particles as they pass the ship stem would be represented in the 2D + T approximation by the wave board acceleration, which was shown here to have a strong affect on crest shape but a weak affect on crest height.

Most wave characteristics appeared to show good correlation for the Slap, Mix and Full wave maker motion categories, with the data from the Fixed cases often being more scattered or sometimes anomalous. Recall that for the Fixed wave maker motion categories, the angle of the wave board relative to vertical varied from 15° to 30° but was held constant throughout each run. The wave crest shape parameters showed a large variation with this fixed angle, with the plunging jet becoming elongated in the horizontal as the wave board angle relative to vertical increased. Interestingly, the contact point heights and the maximum wave heights were largely unaffected by variations in the fixed angle and generally followed the same trends with respect to F_b as the in other wave maker motion categories.

The authors gratefully acknowledge the support of the Office of Naval Research under grants N000140810372 (Program Officer Dr L. Patrick Purtell) and N000140810770 (Program Officer Dr S. J. Russell). The authors are also indebted to Dr M. Tavakolinejad, Dr J. Diorio and Dr X. Liu for their help in setting up and performing the experiments and to Dr F. Noblesse for a number of helpful discussions concerning the interpretation of the results.

REFERENCES

AOKI, K., MASUKO, A., MIYATA, H. & KAJITANI, H. 1982 A numercial analysis of nonlinear waves generated by ships of arbitrary waterline. *J. Soc. Nav. Archit. Japan* **154**, 17–28.

BANNER, M. L. & PEREGRINE, D. H. 1993 Wave breaking in deep-water. *Annu. Rev. Fluid Mech.* **25**, 373–397.

BROCCHINI, M. & PEREGRINE, D. H. 2001 The dynamics of strong turbulence at free surfaces. Part 1. Description. *J. Fluid Mech.* **449**, 225–254.

CALISAL, S. M. & CHAN, J. L. K. 1989 A numerical modelling of ship bow waves. *J. Ship Res.* **33**, 21–28.

CHAPMAN, R. B. 1976 Free-surface effects for yawed surface-piercing plates. *J. Ship Res.* **20** (3), 125–136.

COLAGROSSI, A., LANDRINI, M. & TULIN, M. P. 2001 Numerical studies of breaking bow waves compared to experimental observations, In *Proceedings of the 4th Numerical Towing Tank Symposium., Hamburg, Germany*.

DELHOMMEAU, G., GUILBAUD, M., L DAVID, C. YANG & NOBLESSE, F. 2009 Boundary between unsteady and overturning ship bow wave regimes. *J. Fluid Mech.* **620**, 167–175.

DOMMERMUTH, D. G., O'SHEA, T. T., WYATT, D. C., SUSSMAN, M., WEYMOUTH, G. D., YUE, D. K. P., ADAM, P. & HAND, R. 2006 The numerical simulation o ship waves using Cartesian-grid and volume-of-fluid methods, *26th Symposium on Naval Hydrodynamics, Rome, Italy, 17–22 September*.

DONG, R. R., KATZ, J. & HUANG, T. T. 1997 On the structure of bow waves on a ship model. *J. Fluid Mech.* **346**, 77–115.

DUNCAN, J. H. 2001 Spilling breakers. *Annu. Rev. Fluid Mech.* **33**, 519–547.

FONTAINE, E., FALTINSEN, O. M. & COINTE, R. 2000 New insight into the generation of ship bow waves. *J. Fluid Mech.* **421**, 15–38.

INUI, T. 1981 From bulbous bow to free-surface shock wave – trends of 20 years' research on ship waves at the Tokyo University Tank. *J. Ship Res.* **25** (3), 147–180.

LANDRINI, M., COLAGROSSI, A. & TULIN, M. P. 2001 Breaking bow and stern waves: numerical simulations, In *Proceedings 16th International Workshop on Water Waves Floating Bodies, Hiroshima, Japan*.

MELVILLE, W. K. 1996 The role of surface-wave breaking in air–sea interaction. *Annu. Rev. Fluid Mech.* **28**, 279–321.

MIYATA, H. 1980 Characteristics of nonlinear waves in the near-field of ships and their effects on resistance. In *Thirteenth Symposium on Naval Hydrodynamics*. National Academy Press.

MIYATA, H. & INUI, T. 1984 Nonlinear ship waves. In *Adv. Appl. Mech.*, 24. pp. 215–288.

NOBLESSE, F., HENDRIX, D., FAUL, L. & SLUTSKY, J. 2006 Simple analytical expressions for the height, location and steepness of a ship bow wave. *J. Ship Res.* **50** (4), 360–370.

NOBLESSE, F., DELHOMMEAU, G., GUILBAUD, M., HENDRIX, D. & YANG, C. 2008*a* Simple analytical relations for ship bow waves. *J. Fluid Mech.* **600**, 105–132.

NOBLESSE, F., DELHOMMEAU, G., GUILBAUD, M. & YANG, C. 2008*b* Rise of water at a ship stem. *J. Ship Res.* **52** (2), 89–101.

NOBLESSE, F., DELHOMMEAU, G., KIM, H. Y. & YANG, C. 2009 Thin-ship theory and influence of rake and flare. *J. Engng Maths* **64** (1), 49–80.

NOBLESSE, F., DELHOMMEAU, G., YANG, C., KIM, H. Y. & QUEUTEY, P. 2011 Analytical bow waves for fine ship bows with rake and flare. *J. Ship Res.* **55** (1), 1–18.

OGILVIE, T. F. 1972 The wave generated by a fine ship bow. In *Proceedings 9th Symposium on Naval Hydrodynamics, vol. 2*, pp. 1483–1525. National Academy.

OLIVIERI, A., PISTANI, F., WILSON, R., CAMPANA, E. F. & STERN, F. 2007 Scars and vortices induced by ship bow and shoulder wave breaking. *J. Fluids Engng* **129** (11), 1445–1459.

PELTZER, R. 1984 White-water wake characteristics of surface vessels. *NRL Memorandum Report 5335*. Naval Research Laboratory.

POGOZELSKI, M., KATZ, J. & HUANG, T. T. 1997 The flow structure around a surface piercing strut. *Phys. Fluids* **9**, 1387–1997.

ROBERTS, A. J. 1987 Transient free-surface flows generated by a moving vertical plate. *Q. J. Mech. Appl. Maths* **40** (1), 129–147.

ROTH, G. L., MASCENIK, D. T. & KATZ, J. 1999 Measurements of the flow structure and turbulence within a ship bow wave. *Phys. Fluids* **11** (11), 3512–3523.

SHAKERI, M., TAVAKOLINEJAD, M. & DUNCAN, J. H. 2009*a* An experimental investigation of divergent bow waves simulated by a two-dimensional plus temporal wave maker technique. *J. Fluid Mech.* **634**, 217–243.

SHAKERI, M., MAXEINER, E., FU, T. & DUNCAN, J. H. 2009*b* An experimental examination of the 2D + T approximation. *J. Ship Res.* **53** (2), 59–67.

SONG, W. & MARUO, H. 1993 Bow impact and deck wetness: simulations based on nonlinear slender body theory. In *Proceedings of the 3rd International Offshore and Polar Engineering Conference*, 3. pp. 34–38. International Society of Offshore & Polar Engineers.

STANDING, R. G. 1974 Phase and amplitude discrepancies in the surface wave due to a wedge-ended hull form. *J. Fluid Mech.* **62**, 625–642.

TULIN, M. P. 1957 Theory of slender surfaces planing at high speeds. *Schiffstechnik* **4** (21), 125–133.

TULIN, M. P. & HSU, C. C. 1986 Theory of high speed displacement ships with transom sterns. *J. Ship Res.* **30** (3), 186–193.

TULIN, M. & WU, M. 1996 Divergent bow waves. In *Proceedings of the 21st Symposium on Naval Hydrodynamics*, pp. 661–679. National Academy Press.

TULIN, M. P. & LANDRINI, M. 2000 Breaking waves in the ocean and around ships. In *Proceedings of the 23rd ONR Symposium on Naval Hydrodynamics, Val de Reuil, France*, vol. 4, National Academy, pp. 1–32.

WANIEWSKI, T., BRENNAN, C. & RAICHLEN, F. 2001 Measurements of air entrainment by bow waves. *J. Fluids Engng* **123**, 57–63.

WANIEWSKI, T., BRENNAN, C. & RAICHLEN, F. 2002 Bow wave dynamics. *J. Ship Res.* **46** (1), 1–15.